Machine learning for metallurgy IV: A neural network potential for Al-Cu-Mg and Al-Cu-Mg-Zn

Daniel Marchand and W. A. Curtin
Institute of Mechanical Engineering, École Polytechnique, Fédérale de Lausanne, CH-1015 Vaud, Switzerland

(Received 2 February 2022; accepted 21 March 2022; published 31 May 2022)

Most metallurgical properties, e.g., dislocation propagation, precipitate formation, can only be fully understood atomistically but most phenomena and quantities of interest cannot be measured experimentally. Accurate simulation methods are essential but first-principles density functional theory (DFT) is prohibitively expensive while empirical interatomic potentials are rarely sufficiently accurate for alloys. Machine learning (ML) is emerging as an approach to create computationally-efficient atomistic potentials achieving near-DFT accuracy. Building on recent work on binary Al-Cu and ternary Al-Mg-Si, here a family of neural network potentials (NNPs) for Al alloys of Al-Cu-Mg and Al-Cu-Mg-Zn is developed and assessed using the Behler-Parinello formulation. Training of the potentials uses a robust set of metallurgically-relevant structures including intermetallic phases, stacking faults, solute/solute and solute/stacking fault interactions, solute clusters, and matrix/precipitate interfaces. The accuracy of these NNPs is then demonstrated across a comprehensive set of properties derived from the training set structures and, moreover, many important structures not represented in the training set such as the generalized stacking fault energy (GSFE) surface of the critical S-phase precipitate in Al-Mg-Cu, and antisite and vacancy formation energies for Al-Cu-Mg intermetallics. The broader Al-Cu-Mg-Zn NNPs also have high accuracy for subtle properties such as Cu substitutional energies in the η' and T phases and formation energies of small Al-Zn-Mg clusters. Together with earlier results, this paper shows how increasingly complex multicomponent alloy potentials can be systematically developed by expanding a training database, leading to a comprehensive set of potentials for a broad alloy family, demonstrated here for the technological Al-2xxx, Al-5xxx, and Al-7xxx Al alloys.

DOI: 10.1103/PhysRevMaterials.6.053803

I. INTRODUCTION

The performance-controlling mechanical properties of metals ultimately depend on atomistic details of noncrystalline defects. While these defects, or their effects, can be modeled with high-level approximations such as finite-elements, phase-field, or discrete dislocation dynamics, all such models depend on model parameters that must be estimated by experiments or atomic simulations. For example, precipitates are one of the dominating strengthening features in most engineering aluminum alloys but how these precipitates form (solute clustering, transform path, kinetics) and strengthen (dislocation looping or shearing) can only be quantitatively modeled atomistically. Even within one specific alloy family, e.g., Al-Mg-Zn-Cu Al-7xxx, the complexity across the relevant atomistic configurations required to study just one feature of performance is daunting, making such a scope of studies especially computationally challenging. Thus, methods for atomistic modeling must be both accurate and computationally efficient.

Currently, there are three main approaches to handling the chemical energetics of atomistic modeling that are, in order of increasing computational efficiency, density functional theory (DFT), machine learning interatomic potentials, and semi-empirical potentials such as the embedded atom method. DFT is the most chemically accurate and can capture very subtle features in an alloy, such as the entropic stabilization of the Al-Cu θ phase relative to the θ' [1] phase. However, DFT is very computationally expensive, scaling with the cube of the number of electrons, and so is typically limited to studies of a few hundred atoms even using state-of-the-art supercomputers. This cost rules out direct simulation of complex defects and their interactions in alloys. On the other end of the efficiency spectrum are the semi-empirical potentials (EAM, MEAM, ADP, BOP) that have analytic functional forms and at a cost that scales linearly with the number of atoms. These methods can fit experimental data on basic quantities, but do not have the breadth of quantitative accuracy of DFT. Because of the mathematical structures of these methods, they also have rather limited flexibility to describe alloys, i.e., materials with more than one element. The emerging intermediate path of machine learning involves a very flexible (many-parameter) regression optimization of a large set of training data generated by DFT. The extensive flexibility enables ML potentials to capture many material properties relevant to metallurgy while being extendable to alloys. ML potentials are more expensive than traditional potentials, and must be used cautiously to identify regions where the potential is extrapolating outside the configurational domain of the training data. However, ML potentials for metal alloys are rapidly proving to be quantitatively accurate well beyond the capabilities of traditional potentials while remaining acceptable in cost, as demonstrated in some of our recent papers (Al-Cu [2], Mg [3], and Al-Mg-Si [4,5]). Other recent examples include state-of-the-art potentials for Zn [6], Ti and Zr [7], Fe-H for hydrogen embrittlement [8], Ga/As [9], Hf-O refractory oxide (generated automatically with experimental

input) [10], MoNbTa medium-entropy alloys [11], as well as MoNbTaW and NbMoTaW high entropy alloys [12,13].

The generality of possible ML methods is spawning a wide variety of ML potentials [14–16]. Two essential details enter into the construction of an ML potential: (1) the set of *descriptors* of the local atomistic environments that are the basis on which regression is performed and (2) the scope of the training dataset that is learned by the ML method. These two are not entirely independent—the descriptors should accurately and efficiently capture the atomic configurations of the training set while the training set configurations should span the necessary range of atomic configurations that dictate alloy metallurgy. Descriptors have symmetries with respect to translation, rotation, and substitution, and otherwise should be as orthogonal as possible to span the configuration space. Two main families of descriptors are those of Behler and Parinello [17] and the smooth overlap of atomic orbitals (SOAP) [18] although others such as a cluster expansion [19] and crystal graph networks [20] are emerging. The descriptors are used with some regression scheme, traditionally neural networks for the Behler-Parinello symmetry functions and Gaussian kernels for SOAP, to determine optimal weighting parameters or kernels. New methods that combine the attractive physical basis of the empirical methods and the parameter-rich ML methods are also being developed (PINN) [21,22]. Here, we will use neural network potentials (NNPs) based on the Behler-Parinello formulation and descriptors.

The training sets used to develop ML potentials are often large precomputed custom sets of structures spanning those relevant for the particular problem of interest although potentials created using active learning are becoming popular [10,23–27]. Knowing the many critical subtleties and energetic competitions that must be properly captured for accurate modeling of metallurgical behavior, we believe that the training set should be a curated set of structures spanning all of the relevant structures and defects for the full scope of metallurgical problems in a given alloy. Such an initial training set can then be expanded to improve predictions, if needed, for certain defects or problems of interest. Moreover, as we show here, training sets can be systematically expanded to introduce increasing alloy complexity; e.g. in the family of Al alloys, starting with elemental Al [5], then progressing to binary Al-Cu [2], ternary Al-Mg-Si [4,5] and Al-Cu-Mg (this paper), and quarternary Al-Cu-Mg-Zn (this paper) by adding new training structures with each increase in complexity. In following this approach, we also generate an extensive database that is publicly available for use with any ML method of interest.

Here, we extend our previous development of NNPs in Al, Al-Cu, and Al-Mg-Si to the Al-Cu-Mg and Al-Cu-Mg-Zn systems that constitute the base of the 2xxx (Al-Cu) and 7xxx (Al-Zn-Mg-Cu) alloys, respectively, both of which are technologically important [28]. We start with the Al-Cu-Mg system for which much of the training database was previously computed such that the main new additions are associated with ternary intermetallic phases. This enables the study of the critical S-phase precipitate (sometimes also labeled S' phase) and computation of the generalized stacking fault energy surface relevant for the shearing of S-phase precipitates in an Al matrix. We then build the Al-Cu-Mg-Zn potential, again making use of previous datasets including the Al-Cu-Mg structures. With this potential, we examine Al-Zn-Mg clustering [29] and the impact of Cu on T and η' phase formation energies [30], which were recently studied using DFT. We do not cover all of the vast scope of issues in these alloys, such as early-stage Guinier-Preston-Bagaryatsky (GPB) zones in Al-Cu-Mg studied by Kovarik [31–34] and others [35–40], but the potentials generated here provide the basis for detailed studies of these and other metallurgical aspects in these alloys.

The remainder of this paper is structured as follows. In Sec. II, we summarize the methodology and details of the NNP creation. In Sec. III we comprehensively assess the accuracy of the NNP for essential properties that are represented by structures within the training set. In Sec. IV, we examine the GSFE shearing surface for the S-phase precipitates, the energetics of Al-Zn-Mg clustering, and antisite energies for Al-Cu-Mg compounds. Section V summarizes our paper.

II. METHODOLOGY

A. Atomic structures

For Al-Cu-Mg we start with a database of 11 640 atomic structures, including all Al-Cu structures previously used for an Al-Cu potential [2] and all Al-Mg structures previously used for an Al-Mg-Si potential [4]. We then also include new structures to create the Al-Cu-Mg potential, adding comparatively few structures to show the relative ease with which new potentials can be created by building on prior training sets. The new structures are:

(i) All Al-Mg, Cu-Mg, and Al-Cu-Mg bulk structures from the Open Quantum Materials Database OQMD [41] not previously included in our Al-Cu and Al-Mg-Si potentials

(ii) Al/S-phase interface structures

(iii) Pair and triplet clusters of Al-Cu-Mg elements in 256 atom supercells

(iv) Randomized Mg-Cu structures in FCC supercells

(v) Randomized Al-Mg-Cu structures in FCC supercells

We then use the following structures only for a posteriori validation:

(i) Antisite and Vacancy structures (unrelaxed) for ternary (Al-Cu-Mg) structures in the OQMD

(ii) GSF for the S-phase on the $\{13\bar{1}\}$ and $\{\overline{112}\}$ planes

For the Al-Cu-Mg-Zn potential, we include all the new Al-Cu-Mg training structures and then add:

(i) All Zn-containing compounds (within the Al-Cu-Mg-Zn system) from the Open Quantum Materials Database OQMD [41]

(ii) Dilute solute/solute interactions out to 4 nearest neighbors for all solute pairs in 256 atom supercells

(iii) Surface structures for HCP Zn

(iv) Elastically-distorted Zn structures

(v) Pair and Triplet clusters for Al-Cu-Mg-Zn elements in 256 atom supercells

(vi) Randomized Al-Cu-Mg-Zn structures in FCC supercells

(vii) Randomized Al-Cu-Mg-Zn structures in HCP supercells (using the Zn c/a ratio)

(viii) Fully-relaxed T and η' phases

(ix) Antisite structures for the T and η' phases.

We deviate from our normal practice of not including antisite structures in the training set for this system because, from prior work, we know the Zn→Cu, i.e., Zn replacing Cu, substitution energies are very important for precipitation energetics in the Al-Cu-Mg-Zn system [30].

For the Al-Cu-Mg potential we use the method developed by Imbalzano *et al.* [42] to select the 5820 most diverse structures, i.e., half of the original 11 640, via a furthest-point-sampling (FPS) method. We subsequently show that the remaining 5820 structures have NNP errors that are very similar to those of the chosen most diverse 5820 structures, indicating that no important features are missed by this selection. For the Al-Mg-Cu-Zn interatomic potential we add an additional 4299 structures to the Al-Cu-Mg dataset for a total of 10 119 structures. We do not remove any of these structures using the FPS procedure.

Both the atomic simulation environment (ASE) [43] and Python Materials Genomic (pymatgen) [44] python packages are extensively used to construct and analyze atomic structures.

B. DFT Methodology

All first-principles results are calculated via density functional theory (DFT) as implemented using Quantum Espresso [45] (QE). The GGA-PBE [46] exchange-correlation functional is used with an energy cutoff of 544 eV (40Ry). An 80-k-points/$Å^{-1}$ Monkhorst-Pack grid [47] corresponding to a 20 x 20 x 20 k-point grid for the 4.04 $Å^3$ conventional cubic FCC cell and an 0.6 eV (0.0441Ry) Methfessel-Paxton smearing parameter [48] are used. We use the Al, Mg, Zn, and Cu projector augmented wave (PAW) [49] pseudopotentials of Dal Corso [50]. The Al and Mg pseudopotentials are chosen from the benchmarks of the solid-state pseudopotential (SSSP) library [51] while the Zn and Cu are not the ones chosen by the SSSP but are used because they have fewer valence electrons and thus reduced computational cost relative to those in the SSSP while retaining similar levels of accuracy compared to all-electron benchmarks. We also use AiiDA [52,53] to systematically manage the calculations and to store and search the results; see Ref. [2] for further details. All results in this paper are uploaded to the Materials Cloud [54].

C. NNP methodology

We create neural network potentials (NNPs) with the methods pioneered by Behler and Parrinello [17] and implemented in the open source code n2p2 [55]. Here we outline the basic details of the methodology; further details can be found in the pedagogical review of Behler [56]. The purpose of this paper is to generate broadly useful potentials for Al alloys, and so is not aimed at developing new or enhanced ML methods. Hence, various details below may not be optimal nor rigorously assessed but are fully satisfactory for achieving our goals. As noted earlier, our entire first-principles training set is openly available for use by the community in any other ML development method.

An NNP makes a prediction of the energy of a complete structure by assuming that the total energy can be expressed as a sum of energies E_i^{atom} of each constituent atom,

$$E^{\text{structure}} = \sum_i E_i^{\text{atom}}. \tag{1}$$

The atomic energy E_i^{atom} depends on the local environment of atom i and is hierarchically calculated as a function of weighted neural layers. Here we use an architecture consisting of two hidden layers each with 24 nodes and do not make a study of other possible architectures. Specifically, the E_i^{atom} is computed as

$$E_i^{\text{atom}} = f_3\left(b_1^3 + \sum_{k=1}^{24} a_{k,1}^{2,3}\, f_k^2\left(b_k^2 + \sum_{j=1}^{24} a_{j,k}^{1,2}\, f_j^1 \times \left(b_j^1 + \sum_{i=1}^{N_i^{SF}} a_{i,j}^{0,1}\, G_i\right)\right)\right), \tag{2}$$

where $a_{z,w}^{q,p}$ is the weighting factor from node z on layer q to node z on layer w and b_z^q is the bias of node z on layer q. The f_q are activation functions, here taken as the softplus function $\ln(1+e^x)$ for f_1 with f_2 and f_3 the identity functions. N_i^{SF}, i = Al, Mg, Zn, Cu is the number of symmetry functions for each element.

The functions G_i are the local descriptors of the atomic environment that have the necessary rotational and translational invariance.

Here, we use the two-body radial and three-body (narrow) angular symmetry functions proposed by Behler and Parinello,

$$G_i^{\text{radial}} = \sum_{j=1}^{N_{\text{atom}}} e^{-\eta(R_{ij}-R_s)^2} f_c(R_{ij}) \tag{3}$$

$$G_i^{\text{angular}} = 2^{1-\zeta} \sum_{j\neq i} \sum_{k\neq i,j} [(1+\lambda\cos\theta_{ijk})^\zeta e^{-\eta(R_{ij}^2+R_{ik}^2+R_{jk}^2)} \times f_c(R_{ij})\, f_c(R_{jk})\, f_c(R_{jk})] \tag{4}$$

where R_c, η, ζ, and λ are the symmetry function "hyperparameters", R_{ij} is the distance between atoms i and j, and $f_c(r) = \tanh^3(1 - r/r_c)$ is a cutoff function where r_c is a cutoff distance for each symmetry function. We use the CURSEL method of Imbalzano *et al.* [42] to select a maximally-descriptive set of symmetry functions for the training set. First, we create a dense grid of symmetry functions, 3411 for Al-Cu-Mg and 7264 for Al-Cu-Mg-Zn. Then we run a CUR decomposition, method of producing a using 11 640 structures for Al-Cu-Mg and 10 119 structures for Al-Cu-Mg-Zn. CUR decomposition [57] is a process of creating an approximation of a matrix **X** as a product of matrices **CUR**, where **C** and **R** are composed of a selection of rows and columns of the original matrix **X**. In our use case the matrix X is the response of each symmetry function, as columns, against all the atomic environments as rows. By computing the matrix C we effectively obtain a reduced number of symmetry function to represent the entire system. To compute C, we iteratively determine the "importance" score of individual

columns (symmetry functions) via:

$$\pi_c = \sum_{j=1}^{k} \left(v_c^{(j)}\right)^2, \tag{5}$$

where k is the number of features that to be chosen and $v_c^{(j)}$ is the cth coordinate of the jth right singular vector. We refer the reader back to the work of Imbalzano *et al.* [42] for further details regarding the method. For both Al-Cu-Mg and Al-Cu-Mg-Zn we also add all five 3-body Al-centered symmetry functions from the our prior work on Al-Mg-Si [4] because we find that we otherwise cannot reasonably reproduce the C_{44} elastic constant of Al. For the Al-Cu-Mg potential we find that using 64 SFs per element, plus the five previously-used 3-body Al SFs was sufficient, for a total of 197 SFs that are listed in Tables I and II in Appendix A. For the Al-Cu-Mg-Zn potentials, we find that 96 SFs per element, for a total of 389 SFs (including the extra 3-body Al SFs), are needed for sufficient accuracy; these are also listed in Tables III–V in Appendix A.

Training of the NNP potential, i.e., determination of the weights and biases to best-match the DFT reference data, is handled by the n2p2 library [55,58]. We select at random 90% of the structures for training and the remainder for testing. NNP weights are updated during the training using a fading memory Kalman filter with code parameters $\epsilon = 0.07$, $\lambda = 0.985$, and $\nu = 0.9987$ and we do not use the noise parameter q. The training is based on minimizing an objective, or loss, function Γ^{loss} based on the total energies E_i of each structure in the training set and the atom forces force on the j^{th} atom denote $F_{i,j}$ and computed by

$$\Gamma^{\text{loss}} = \frac{1}{N^{\text{struct}}} \sum_{i=1}^{N^{\text{struct}}} \Big(\left(E_i^{\text{NNP}} - E_i^{\text{DFT}}\right)^2 + \frac{\beta}{3N_i^{\text{atom}}} \sum_{j=1}^{3N_i^{\text{atom}}} \left(F_{i,j}^{\text{NNP}} - F_{i,j}^{\text{DFT}}\right)^2 \Big), \tag{6}$$

where the sum is over all input training structures N^{struct}. We tune the relative importance of forces and energies in the total loss via the parameter $\beta = 8(\text{Å}^2)$. Since each training structure provides one total energy but $3N_i^{\text{atom}}$ forces, we use only a fraction 2.1% of the forces, randomly selected, during each iteration of training. Decreasing this ratio results in a loss of accuracy while increasing the ratio becomes computationally expensive. This approach is not perfect since it introduces a bias toward larger (more atoms) structures.

In standard machine learning, a common practice is to use "early stopping" wherein training is halted when the errors for structures in the testing set begin to increase, indicating the start of possible overfitting. For NNPs, this procedure is challenging since the energies converge faster than the forces. As a compromise, we use a fixed 150 iterations [2] and find that the iterations in the range of 60 to 300 does not substantially affect the results.

Using the above framework, our initial Al-Cu-Mg-Zn potentials struggled to accurately capture the formation energies of Zn-containing compounds, particularly binary and triplet compounds. This was traced mainly to inaccuracy in predicting the energy of dilute Zn in the Al matrix. Adding additional Zn-in-Al structures does not ameliorate the problem. To overcome this issue we perform a second round of training, after training on the entire dataset, on a smaller targeted training set of 287 structures focused on dilute Zn and Cu-Mg-Zn triplet structures embedded in Al. We term this process of training the neural network on a subset of the data to improve specific properties after initial training on the entire dataset "secondary training". This process is somewhat similar to transfer learning [59], wherein a neural network trained on one task is retrained on another similar task afterwards. We do not use this term, however, to emphasize that we are trying to improve performance on a subset of the original training set rather than boost performance on a different task altogether. Because we wish to alter our neural network as little as possible, i.e., to tune it to our targeted training set without impacting broad properties, we alter our Kalman filter settings to make it more "gentle" by increasing the ϵ parameter from 0.07 to 0.5, where ϵ is effectively an inverse of the "learning rate" in standard gradient descent (see the analysis of Luttmann *et al.* [60]). We also do not use forces during secondary training as using them destroys the quality of the potential w.r.t. properties in the original dataset. We also switch from a fading memory to a standard Kalman filter and set the η parameter, which does not exist in fading memory Kalman, to 0.01 and use zero noise ($q = 0$), we do this to make our Kalman filter settings more directly in line with the analysis of Luttmann *et al.* Finally we train for only one epoch, as while training for additional epochs results can result in further improvements in the target dataset it comes with the cost of degradation of properties in the original dataset. The results are sensitive to choice of Kalman filter during secondary training, in particular, should ϵ be too high (effective learning rate low) or the number of epochs too few, then secondary training has little impact and the properties of interest remain poor, however, too low of an ϵ (learning rate high) or too many epochs, will cause degradation of properties in the full training set.

Using the above procedures and settings, we have created 20 NNPs each for the Al-Cu-Mg and Al-Cu-Mg-Zn systems. We use n2p2 via a plugin to LAMMPS [61] to execute simulations and in most cases use the atomic simulation environment (ASE) interface [43]. We report the average and standard deviation for values across all NNPs (noting that the NNPs are not statistically independent; accurate statistical analysis requires models such as that developed by Musil *et al.* [62]). When we report specific neural networks we label them with the alloy followed by a neural network index, e.g., AlCuMgZn-NNP7 refers to seventh AlCuMgZn neural network potential. Postprocessing uses the Numpy [63] and Scikit-learn [64] python packages in Jupyter notebooks [65], atomistic figures are plotted with Ovito [66] and graphs are constructed with the Matplotlib [67].

III. RESULTS: NNP VERSUS TRAINING AND TEST DATA

A. Overall NNP accuracy

The accuracy of each NNP is assessed using the root mean square error (RMSE) for energies and forces for structures in

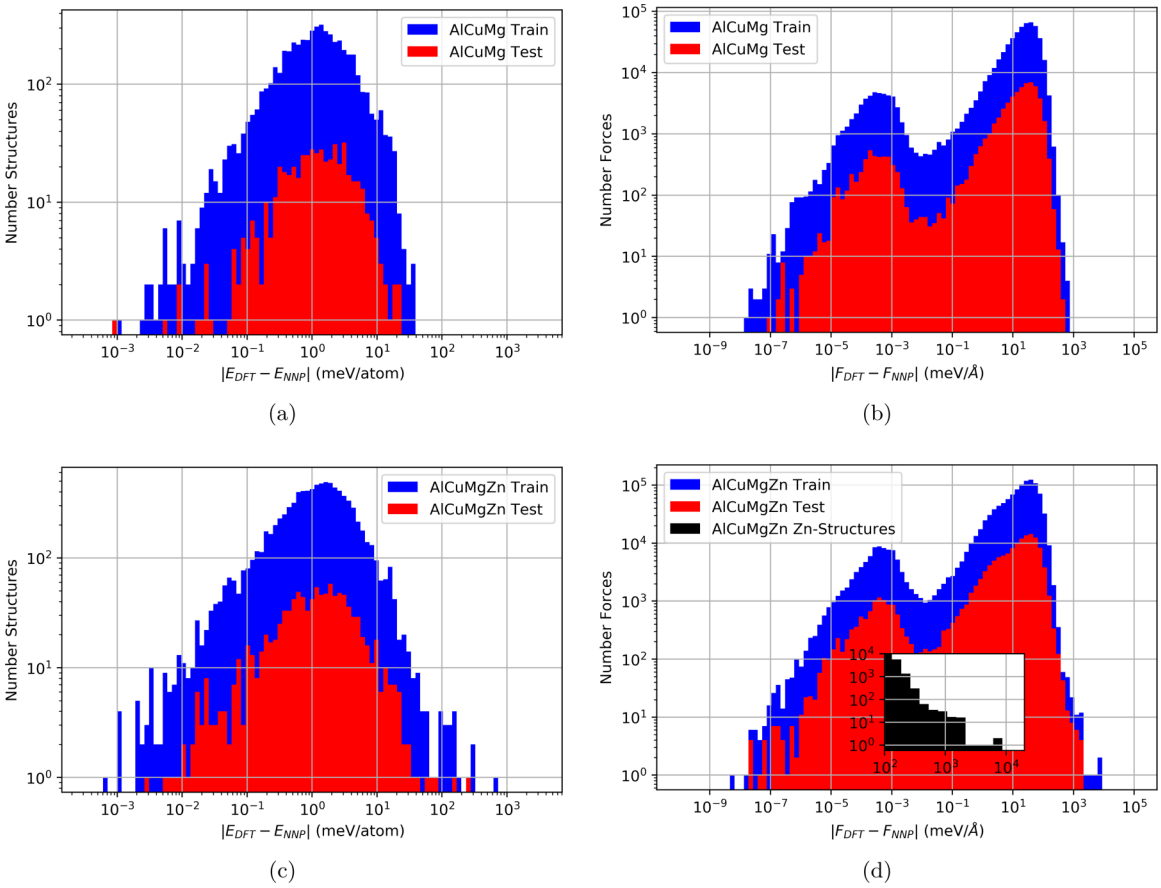

FIG. 1. Histogram of errors for the (a) energy and (b) forces for training (blue) and testing (red) for AlCuMg-NNP1. The energy (c) and force (d) errors for the AlCuMgZn-NNP1 potential for training (blue), test (red) and, for the forces, all Zn-containing structures (black, inset). The AlCuMgZn results are prior to secondary training on the focused dataset, a comparison of train/test errors of NNP1 before/after secondary training is in Appendix D.

the testing and training set and is defined as

$$\mathrm{RMSE}(E) = \left(\frac{1}{N^{\mathrm{struct}}} \sum_{i}^{N^{\mathrm{struct}}} \left(E_i^{\mathrm{DFT}} - E_i^{\mathrm{NNP}} \right)^2 \right)^{\frac{1}{2}}, \quad (7)$$

$$\mathrm{RMSE}(F) = \left(\frac{1}{N^{\mathrm{struct}}} \sum_{i}^{N^{\mathrm{struct}}} \sum_{j}^{3N_i^{\mathrm{atom}}} \frac{1}{3N_i^{\mathrm{atom}}} \left(F_{i,j}^{\mathrm{DFT}} - F_{i,j}^{\mathrm{NNP}} \right)^2 \right)^{\frac{1}{2}}. \quad (8)$$

For the Al-Cu-Mg potentials the average RMSE for energies across all 20 NNPs is 3.90 meV/atom in the training set and 5.51 meV/atom in the testing set. The RMSE for the forces is 40.5 meV/Å in the training set and 71.9 meV/Å in the testing set. The high average testing errors, particularly for the forces, across all Al-Cu-Mg NNPs are due mainly to a few of the NNPs, with AlCuMg-NNP7 having a force test error of 645 meV/Å. Excluding AlCuMg-NNP7, the average RMSE for force test errors drops to 41.73 meV/Å. In Fig. 1 we show the error in the (a) energies and (b) forces for AlCuMg-NNP1. We also perform t-SNE to create an embedded mapping of the results to get an overall sense of how which structures are removed via FPS and where the distribution of errors lie, this analysis is shown in Appendix B along with the t-SNE plot in Fig. 19.

For the Al-Cu-Mg-Zn potentials, prior to secondary training, the average RMSE across all potentials for energies is 11.03 meV/atom in the training set and 32.00 meV/atom in the testing set while the RMSE for forces is 41.28 meV/Å in the training set and 66.69 meV/Å in the testing set. The large 32.0 meV/atom test error for energies is not typical, with half of the NNPs having a test less than 13 meV/atom. Looking more closely at AlCuMgZn-NNP1 in Fig. 1(c), the large energy errors are mainly due to relatively few outliers. The energy RMSE for all structures (test + train) is 11.54 meV/atom, but with the 10 largest-error structures (0.1% of total) removed, it is only 6.27 meV/atom while with the 30 largest-error structures (0.3% of total) removed it is 4.56 meV/atom. The structures of all the major outliers for AlCuMgZn-NNP1 are ZnCu (P63mc), MgZn (Pmc21), Zn3Cu2 (R-3c), and MgZn (P63mc), or, are a structure derived from them, e.g., via volumetric dilation, and all of which have high formation energies and hence are of very little practical relevance. While the forces have an overall moderate RMSE, some individual errors may be quite high, referring to the histogram of force errors in Fig. 1(d), where we see a substantial number of structures with errors >500 meV/Å, always for Zn-containing structures. These errors come from the following sources (1) structures with very high formation energies, that are unlikely to come up in practical use, (2) structures with high forces overall and in which the NNP

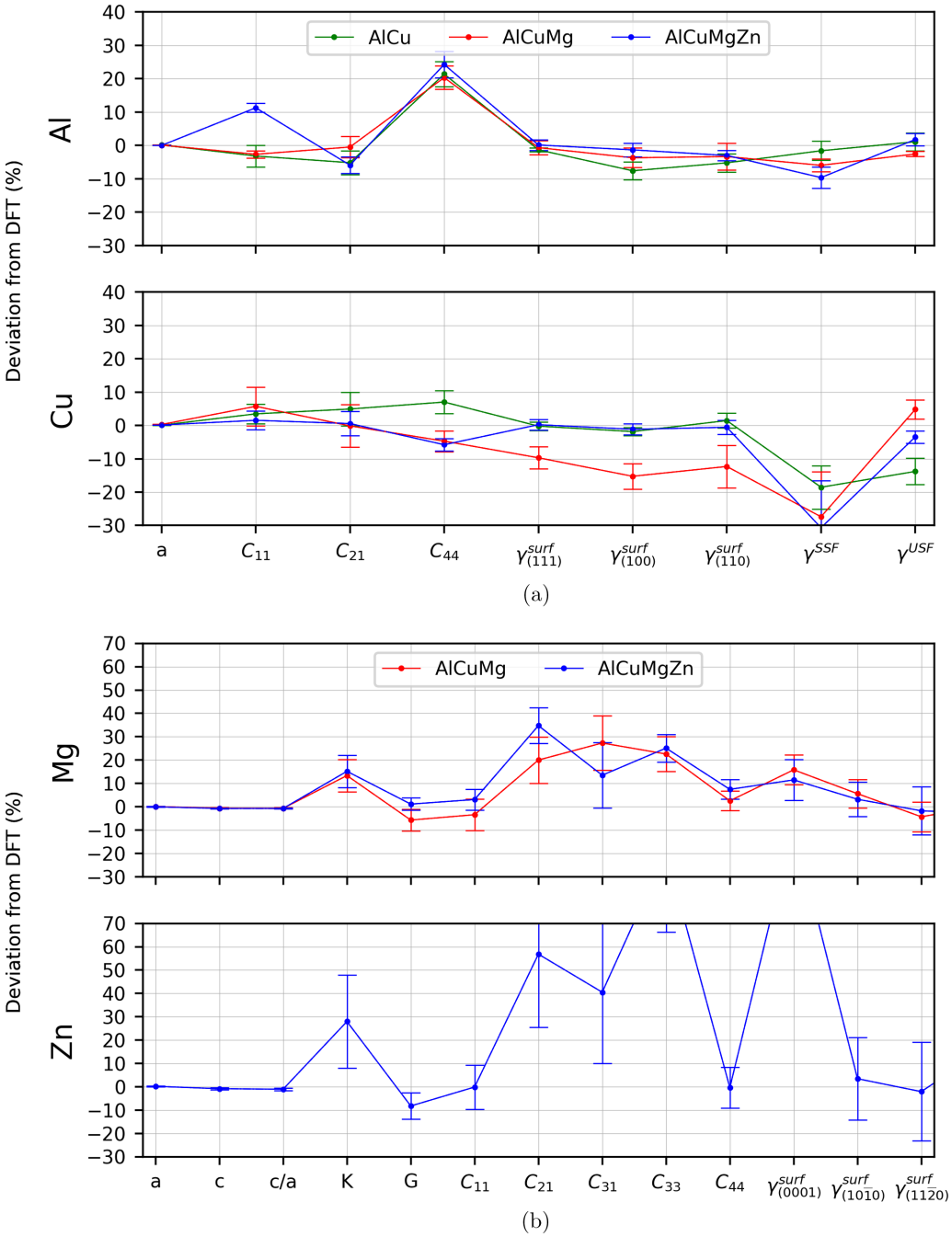

FIG. 2. Deviation of NNPs from DFT reference values (%) for lattice constants, elastic constants, surface energies, for FCC Al and Cu (a) and HCP Mg and Zn (b) figure (a) also includes and stable and unstable stacking fault energies. All structures from which these properties are derived are included in the training set.

forces are within ≈10% their DFT values, and (3) intermediate states in the transition between η' structures. In Fig. 20 of Appendix C, we go into greater detail for an example of case (3) during a relaxation of an antisite-containing η'_I structure.

For Al-Cu-Mg-Zn potentials after secondary training, the energy and force errors increase but do not change significantly. For AlCuMgZn-NNP1 specifically, the secondary training increases energy errors on the original train and test datasets from 11.54 meV/atom and 11.52 meV/atom to 12.68 meV/atom and 12.72 meV/atom respectively, and for the force errors barely from (train/test) 42.94 meV/Å/45.53 meV/Å to 43.07 meV/Å/45.67 meV/Å, after secondary training. The histogram of error distribution before/after secondary training can be seen in the Fig. 21 of Appendix D. As mentioned, we perform secondary training on a targeted dataset to improve the quality of dilute solution energies, in Fig. 22 of Appendix E, we confirm that the process does indeed improve the accuracy. Furthermore, we rigorously compare the material properties before and after secondary training and find that secondary training does little (aside from improving dilute solute energies) (see Supplemental Material [68]).

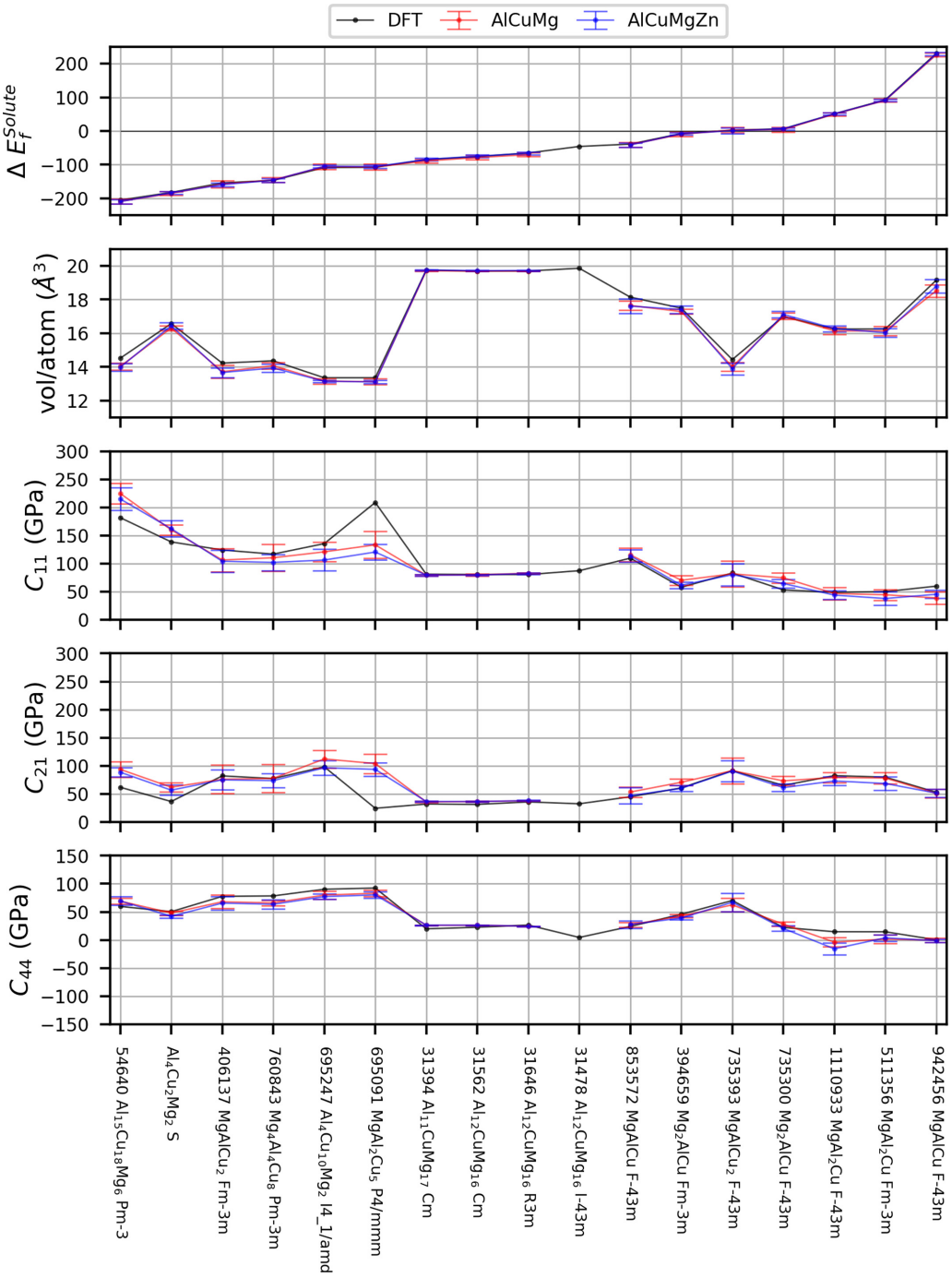

FIG. 3. Formation energy, atomic volume, and elastic constants C_{11}, C_{21}, and C_{44} as predicted by DFT, and the NNPs versus structure, for all Al-Cu-Mg structures in the OQMD database. All structures from which these properties are derived are included in the training set.

B. Elemental bulk properties

Figure 2 shows the relative deviation of NNP results from the DFT references values for fundamental properties of elemental Al, Cu, Mg, and Zn, using the various NNPs. As found in earlier NNPs for Al, the C_{44} in Al is challenging to model accurately [2,4], with the NNPs consistently overestimating C_{44} by 20%. The DFT reference is not a source of error because the DFT settings were carefully converged with respect to Al C_{44}. Elastic constants are challenging to capture because they are second derivatives of the energy and, therefore, most sensitive to any noise or error, and indeed the errors here are consistent with other NNPs in the literature [69]. The NNP for Zn is particularly poor at modeling C_{33}, but this has also been very challenging for classical potentials until the work of Dickel *et al.* [70]. Interestingly, Dickel *et al.* mention that it is typically very challenging to capture the c/a ratio for Zn while the current NNPs are extremely accurate (1% relative error).

C. Bulk properties

Figures 3–6 show the formation energies, atomic volumes, and elastic constants for all Al-Cu-Mg, Al-Mg, Cu-Mg and

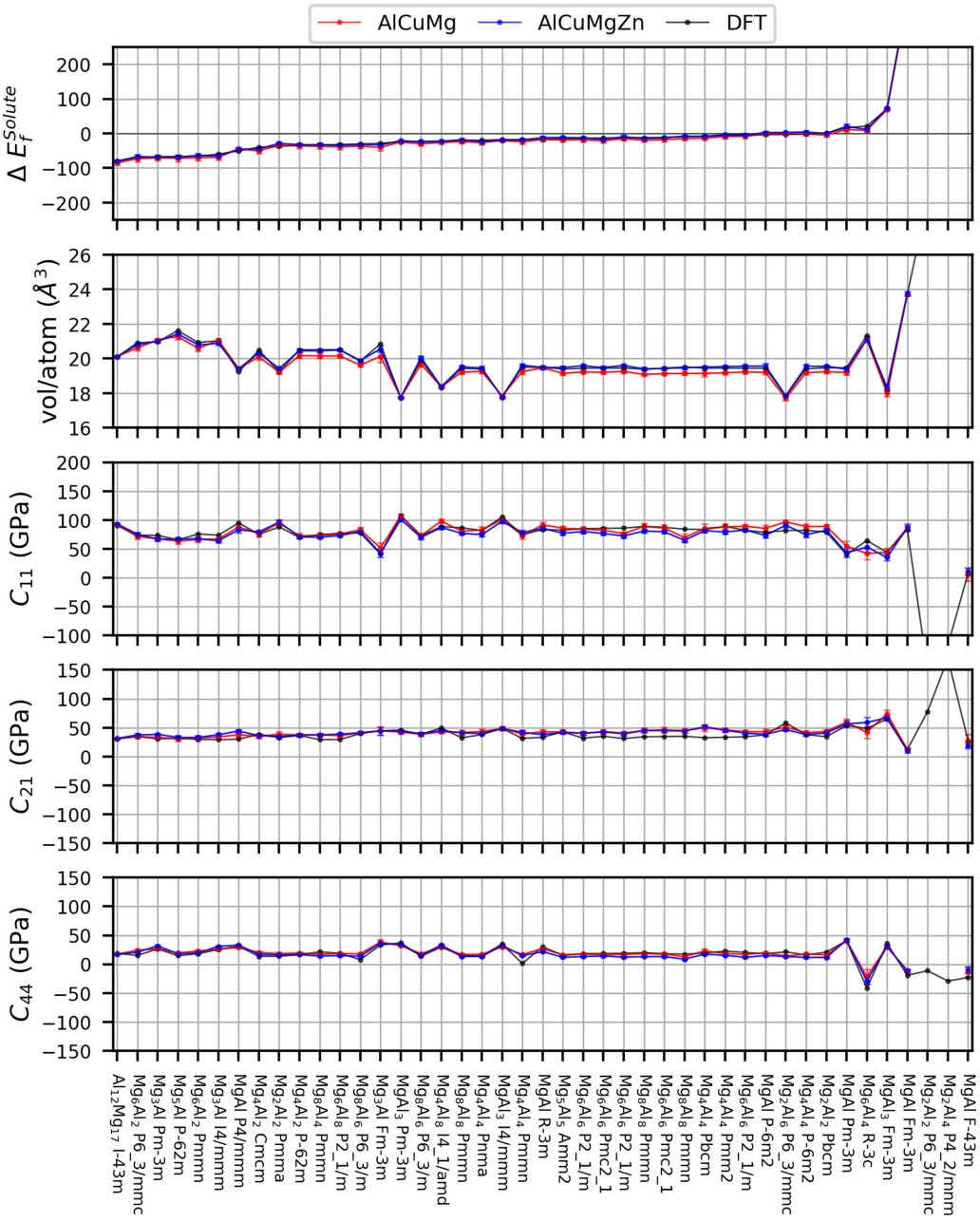

FIG. 4. Formation energy, atomic volume, and elastic constants C_{11}, C_{21}, and C_{44} as predicted by DFT, and the NNPs versus structure, for all Al-Mg structures in the OQMD database. All structures from which these properties are derived are included in the training set.

Al-Cu intermetallic structures within the OQMD database as computed via DFT and the NNPs developed in this paper, in 6 we also include results form our previously-developed Al-Cu NNP.

The formation energy $\Delta E_f^{\text{structure}}$ of each structure is computed relative to the reference energy E_X^{SS} for bulk FCC Al and dilute Cu, Mg, and Zn solid-solutions in Al matrix as

$$E_X^{SS} = E_{\text{Al}_{M-1(X)}} - (M-1)E_{\text{Al}_M}/M, \quad (9)$$

where $X =$ Mg, Cu, Zn with E_{Al_M} and $E_{\text{Al}_{M-1(X)}}$ the total energies of supercells containing M Al atoms and $(M-1)$ Al atoms and one atom of X, respectively. The energy $E^{\text{tot}}_{\text{Al}_{M-1(X)}}$ is computed using a 4 x 4 x 4 supercell of the cubic FCC cell (256 Al atoms) with the volume held fixed. The formation energy $\Delta E_f^{\text{structure}}$ of any other structure is then computed as

$$\Delta E_f^{\text{structure}} = \left(E^{\text{tot}}_{\text{Al}_X\,\text{Mg}_Y\,Cu_Z} - \sum_{X=\text{Al,Mg,Cu}} n_X E_X^{SS} \right) \Big/ N, \quad (10)$$

where $E^{\text{tot}}_{\text{Al}_X\,\text{Mg}_Y\,\text{Cu}_Z}$ is the total energy of a precipitate unit cell containing X Al atoms, Y Mg atoms, Z Cu atoms and $N = X + Y + Z$ the total number of atoms, where all atomic positions are fully relaxed. We only plot the NNP results when they relax to the same spacegroup as DFT as sometimes they relax to a lower-energy configuration, e.g., in Fig. 4, Mg_2Al_2 P6_3/mmc the NNP results are not displayed as all the NNPs

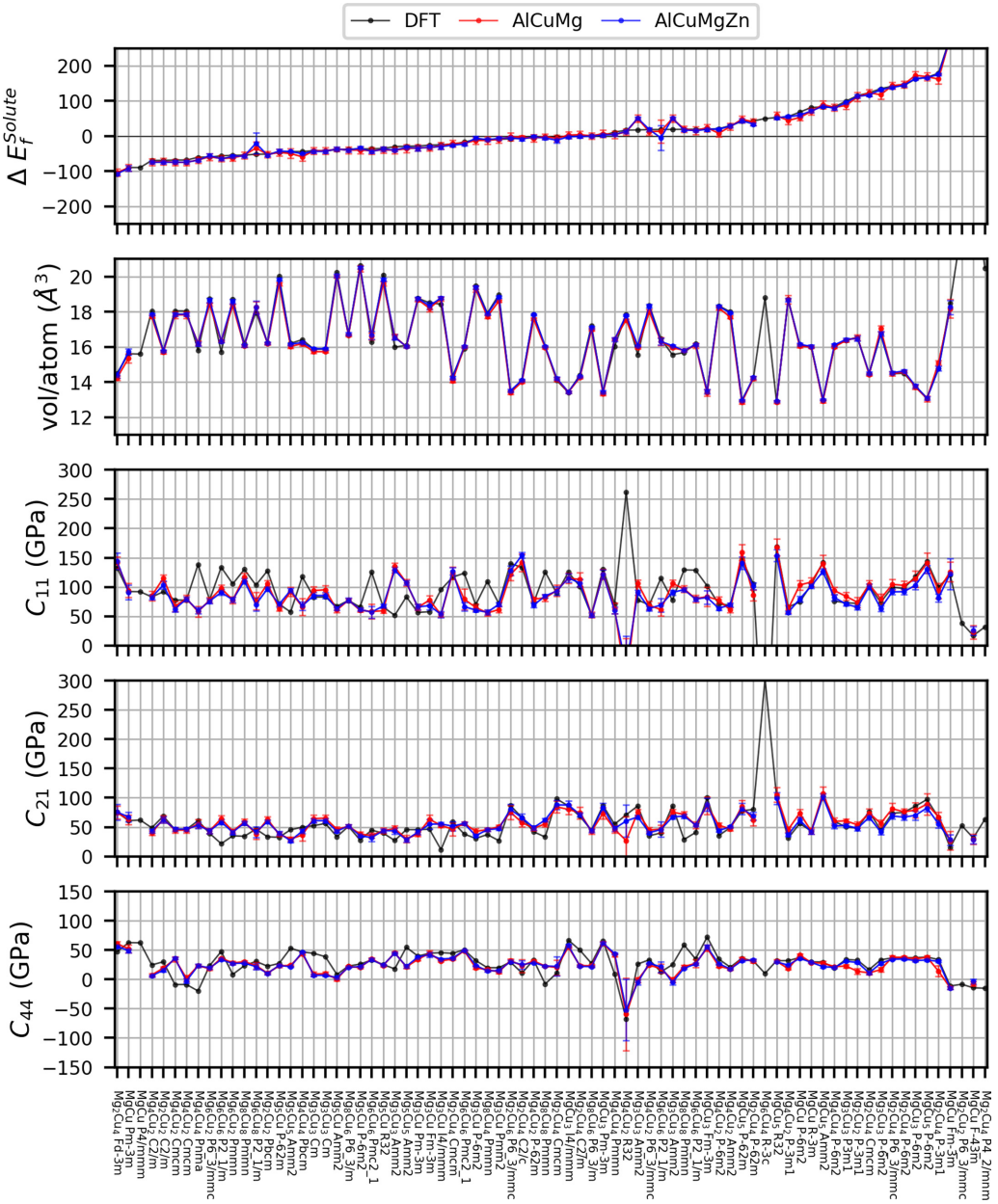

FIG. 5. Formation energy, atomic volume, and elastic constants C_{11}, C_{21}, and C_{44} as predicted by DFT, and the NNPs versus structure, for all Cu-Mg structures in the OQMD database. All structures from which these properties are derived are included in the training set.

relax the structure into one of the lower-energy spacegroups of the same stoichiometry, e.g., Pmmn and R-3m.

In general, the Al-Cu-Mg potential performs very well across a very diverse and comprehensive set of structures including the Al-Cu, Al-Mg, and Cu-Mg binaries as well as the Al-Cu-Mg ternaries. The larger errors tend to be only for structures that are not thermodynamically stable with respect to solid solution, or are mechanically unstable, i.e., have negative elastic constants. In particular, we find that the NNP-predicted formation energies and atomic volumes are usually very close to the DFT values. As before, we note the poorer performance of the NNPs in predicting the elastic constants. Despite the increased complexity of modeling a ternary Al-Cu-Mg potential, the results in Fig. 6 are comparable to those of our previous binary Al-Cu potential [2]. Results are also shown for the binaries and ternaries as predicted by the Al-Cu-Mg-Zn NNP, and are comparable to those for Al-Cu and Al-Cu-Mg. Hence, no fidelity is lost upon expansion of the dataset to include new elements (Mg added to Al-Cu, and Zn added to Al-Cu-Mg). Furthermore, as shown in Fig. 7 and Figs. 23–28 in Appendix F, for all Zn-containing compounds within the OQMD, the NNPs reproduce the atomic volume and formation energy very well with only a few exceptions for compounds that have high formation energy but preserving the overall trend.

D. Solutes

We compute the solute-solute formation energies (interaction energies) again using Eq. (10). The DFT and NNP results for all solute pairs are shown in Fig. 8 with the NNPs generally

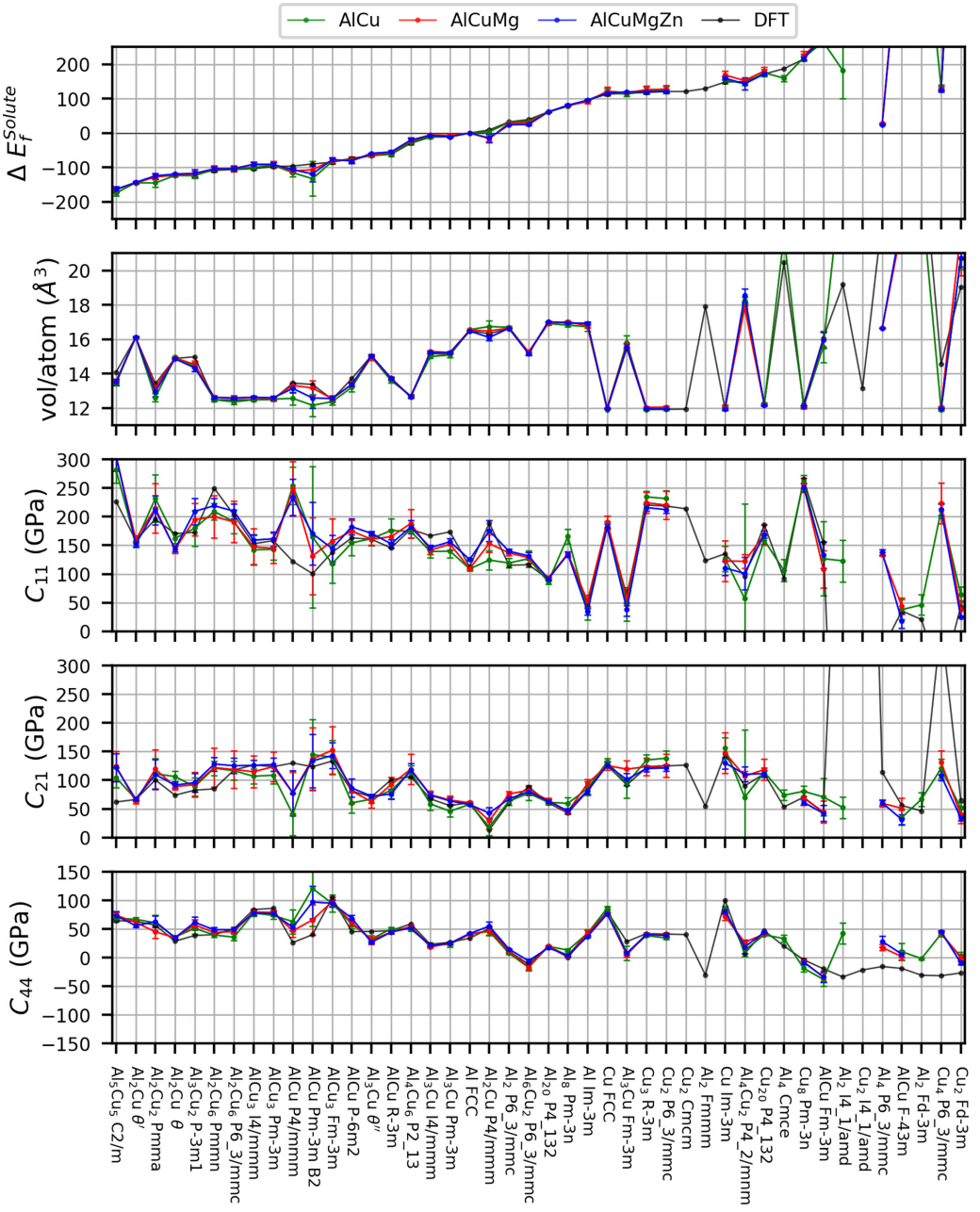

FIG. 6. Formation energy, atomic volume, and elastic constants C_{11}, C_{21}, and C_{44} as predicted by DFT, and the NNPs versus structure, for all Al-Cu structures in the OQMD database. All structures from which these properties are derived are included in the training set.

in good agreement with DFT, typically well within 25 meV (≈kT at room temperature). Notable deviations are found only for the nearest-neighbor Cu-Vac and Mg-Vac binding energies. The NNP Cu-Vac energies are slightly positive while the DFT value is slightly negative but the absolute deviation remains 25 meV. The NNP Mg-Vac energy is in the range of –20 to –35 meV, as compared to the DFT value of only –5 meV, so that the tendency for Mg-Vac binding is overpredicted.

We next examine Mg-Cu-Zn solute triplet cluster formation energies, again using Eq. (10) as shown in Fig. 9. Two configurations are examined, one labeled (111) with all three solutes as near-neighbors on the (111) plane and another labeled (112) with the three solutes on a (100) plane as shown schematically in the figure. Overall, both Al-Cu-Mg and Al-Cu-Mg-Zn NNPs capture the broad trend exhibited by the DFT results. Quantitatively, most energies are within 25 meV but the results for Al-Cu-Mg-Zn are systematically less negative than the DFT. The ternary Al-Mg-Cu NNP is closer on average to the DFT for most configurations, but notably higher for the lowest-energy CuCuCu-112 structure. Hence, early stage clustering and the competition between 111 and 112 structures would not be well-represented with the Al-Mg-Cu NNP although the Al-Cu-Mg-Zn NNPs have more accurate energy differences for most of these clusters, due to, as discussed in the methods, triplet structures being included in the secondary-training dataset for these potentials. Finally, across the full spectrum of NNPs, there is substantial scatter, with some deviating

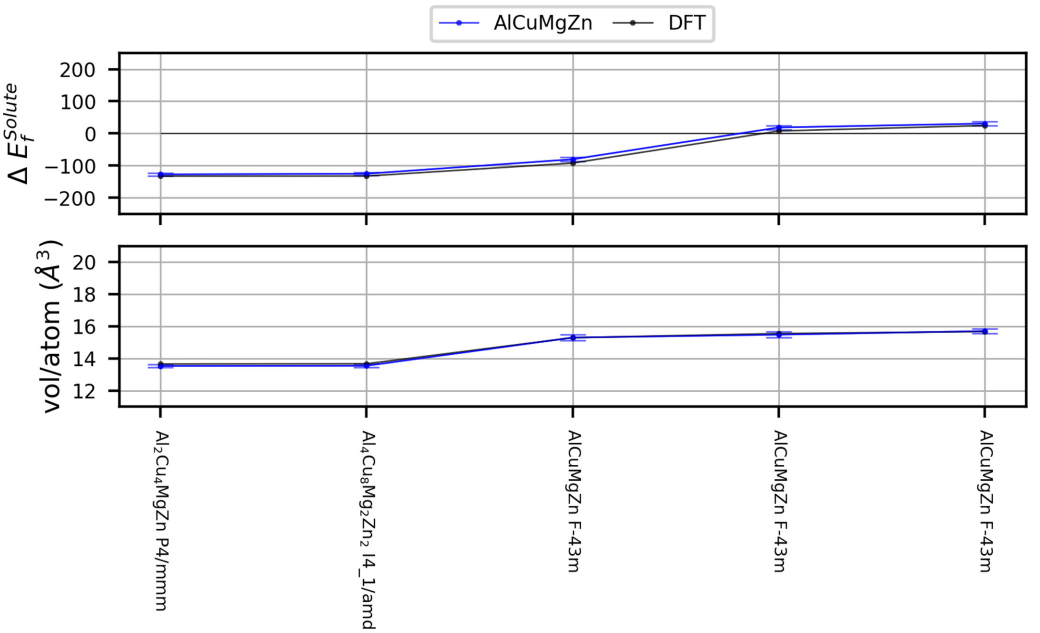

FIG. 7. Formation energy and atomic volume as predicted by DFT, and the NNPs versus structure, for all Al-Cu-Mg-Zn structures in the OQMD database. All structures from which these properties are derived are included in the training set.

by 50 meV or more from DFT. This suggests that using a committee model [71], i.e., averaging across multiple NNPs, might be a very useful approach for early stage cluster evolution.

The solute misfit volumes are important for solute/dislocation interactions and consequent solute strengthening in the solid solution state. We compute the solute misfit volume Δv_m as [73]

$$\Delta v_m = \left(\frac{1}{B}\frac{\delta p}{\delta c}\right), \tag{11}$$

where B is the Al bulk modulus and $\frac{\delta p}{\delta c}$ the slope of the cell pressure vs solute concentration in the computational cell. Here, we compute the pressure created by a single solute introduced into a 256-atom Al cell. Figure 10 shows the misfit volumes for Cu, Mg, Zn, and the Vacancy in Al, as predicted by DFT and the NNPs. The NNPs show good accuracy, although with slightly larger misfit volumes for Cu for the Al-Cu and Al-Cu-Mg potentials.

Figure 11 shows the solute/stacking fault interaction (sol-SF) energies for Cu, Mg, and Zn solutes in Al in order of their distance to the SF plane, here we present the four closest sites to the SF plane, SF index 1 is the closest site, SF index 2 is the second closet. This interaction energy between solute and stacking fault, E_{X-SF} is computed as

$$E_{X-SF} = E_{N-1,X}^{\mathrm{Sol-SF}} - E_N^{\mathrm{SF}} - \left(E_{N-1,X}^{\mathrm{1sol}} - E_N^{\mathrm{Pure}}\right), \tag{12}$$

where $E_{N-1,X}^{\mathrm{Sol-SF}}$ is the energy of a system containing the stacking fault and a single solute, (X = Cu, Mg, Zn) and E_N^{SF} is the energy of the system with the stacking fault alone. $E_{N-1,X}^{\mathrm{1sol}}$ and E_N^{Pure} are the energies of a structure of the same number of atoms as the SF-containing one but without the defect and containing one solute, or of pure Al matrix respectively. There is general agreement between the NNPs and DFT but some deviations. For Cu, DFT shows a small third-plane attraction of –18 meV while the NNPs are around zero. For Mg, DFT shows a small second-plane attraction while the NNPs show a small repulsion. Most of the interaction energies are quite small, below 20 meV in magnitude, so that practical effects are negligible, except for Cu in the first two planes where the energy is larger and for which the NNPs perform fairly well.

E. Interface and generalized stacking fault energies

Modeling of interfaces is essential for a metallurgically-relevant atomic potential in two ways: (1) a dislocation passing through a precipitate must first pass through the interface and (2) the thermodynamics of precipitate formation depends on the precipitate/matrix interface energies. Interface energies are rarely considered when fitting EAM-style potentials and consequently are poorly predicted. Interfaces are challenging to accurately predict because often there is a dearth of a experimental information of their structure, which can often include substantial restructuring or relaxation. However, approximate structures can be insightful in providing guidance and potentials trained on approximate structures can be used to assist in the discovery of lower-energy structures with the same nominally geometry.

We use the methods in Ref. [2], based on [74], as summarized here. For a structure containing an interface, with N atoms total, of which there are X atoms of matrix and Y atoms of precipitate, the formation energy $\Delta E_{f,(X,Y)}^{\mathrm{interface}} = E_{X,Y}^{\mathrm{interface}} - XE_{\mathrm{bulk}}^{\mathrm{Matrix}} - YE_{\mathrm{bulk}}^{\mathrm{Precip}}$, is related to the number of atoms as

$$\Delta E_{f,(X,Y)}^{\mathrm{interface}} = \delta E_{X,Y}^{\mathrm{strain}} + \frac{2A\gamma^{\mathrm{interface}}}{N}, \tag{13}$$

where $\Delta E_f^{\mathrm{interface}}$ is the interface formation energy, $\delta E_{\mathrm{strain}}$ is the strain energy, A the surface area, γ^{int} the interface energy, and $N = X + Y$ the total number of atoms in the interface-

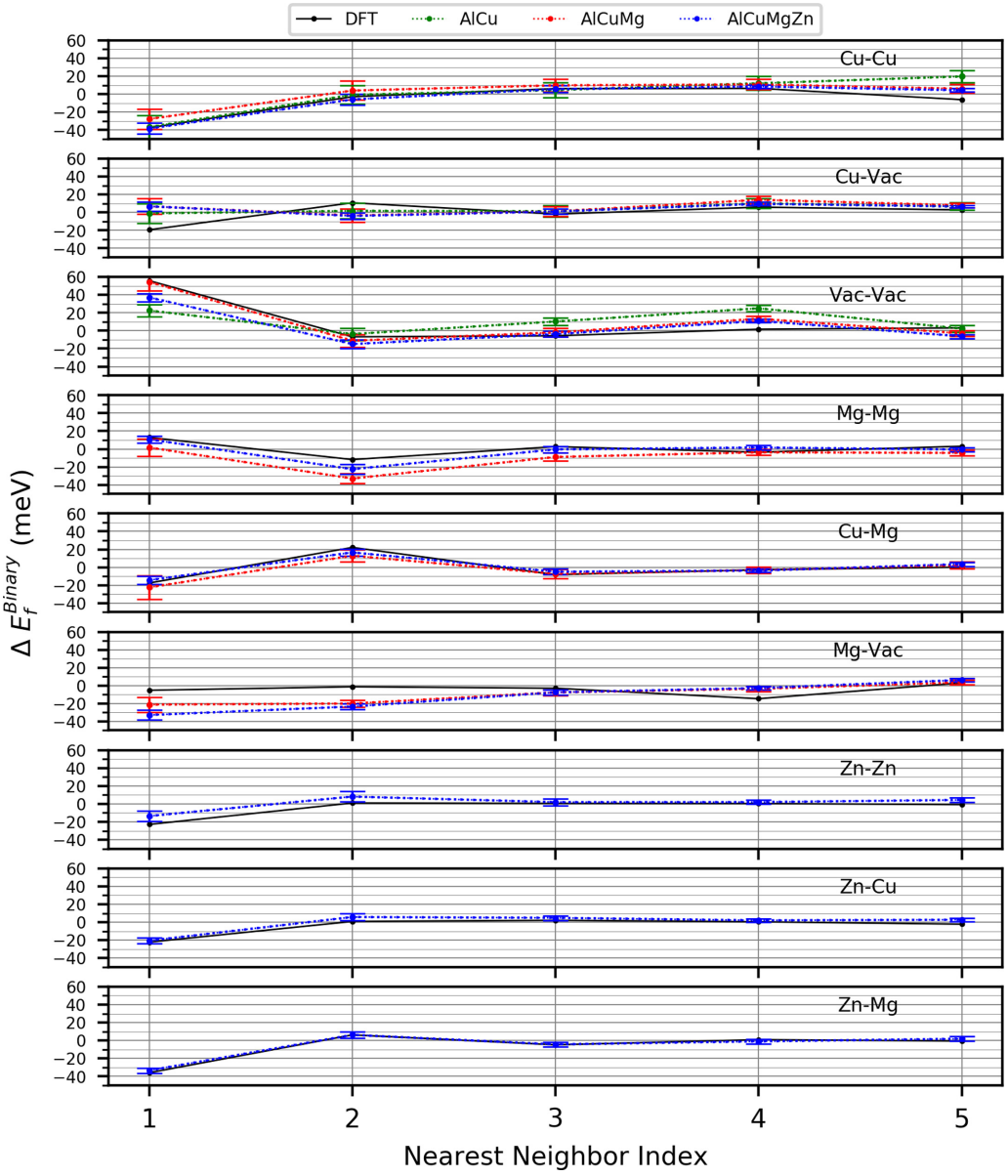

FIG. 8. Binary solute formation binding energies for Cu, Mg, Zn, and Vac binary pairs in an Al matrix as a function of nearest neighbor index. These structures are included in the training set.

containing structure. When computing $E_{X,Y}^{\text{inteface}}$, the atoms are free to fully relax while the cell is held fixed in size and shape. The interface surface energy $\gamma^{\text{interface}}$ is then the slope of $\Delta E_f^{\text{interface}}$ versus $\frac{1}{N}$ and divided by $2A$.

We generate the S-phase/Al interface having a $(012)_{Al}\|(001)_S$ habit plane using the method in Liu *et. al* [75]. Figure 29 in Appendix G, we show the structure of the S phase in detail along with the numerical results we use to compute the interface energy. Figure 12 shows the interface energy, as well as those for various Al-Cu θ' and θ'' interfaces studied previously [2]. The NNPs predict all of these interface energies in good agreement with DFT.

We also benchmark the potentials against θ and θ'' generalized stacking energy surface and find the results to be in very good agreement with DFT and as accurate as our previously-developed Al-Cu potential, as can be seen in Figs. 30 and 31 in Appendix H.

F. Antisites for η' and T phase

We next move to the quarternary Al-Mg-Zn-(Cu) system and compare the NNP predictions to our recent DFT results on antisite energies in two important phases in this alloy alloy [30]. The two key phases are the η' and T phases, which are found experimentally to form more easily upon the addition of a small amount of Cu. DFT shows that the Cu substitutions lower the formation energy of these precipitates. We compute the substitutional energies, $E_{\text{substitution}}$ in the same manner we later compute the antisite energies, $\Delta E_f^{\text{antisite}}$ via:

$$\Delta E_f^{\text{antisite}} = E^{\text{antisite}} - E^{\text{pristine}} - E_{\text{new}}^{\text{ref}} + E_{\text{old}}^{\text{ref}}, \tag{14}$$

where E^{antisite} and E^{pristine} are precipitate energies with and without the defect (antisite or vacancy) and $E_{\text{new}}^{\text{ref}}$, $E_{\text{old}}^{\text{ref}}$, are new and old element reference energies as shown in Eq. (9).

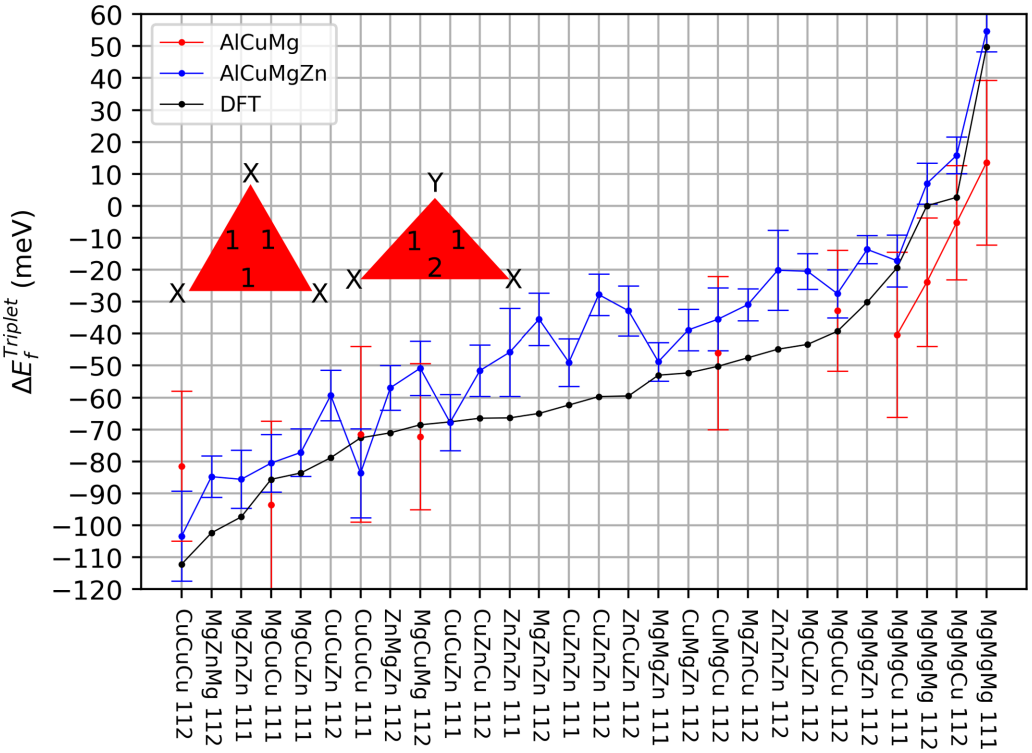

FIG. 9. Triplet formation energies for Cu-Mg-Zn triplets in an Al matrix. We label all triplets by the lengths of their bonds, in the same manner as Gorbatov *et al.* [72] 111 indicates all nearest neighbors, and 112 indicates two nearest neighbors and one second-nearest neighbor, see schematic on the figure. For the 111 triplets, all positions are the same and the order of the elements does not matter, e.g., AlMgCu 111 = CuMgAl 111 = AlCuMg 111. For the 112 triplets, there are two different sites: one that is surrounded by two nearest neighbors, marked as Y on the schematic, and two that are surrounded by one nearest neighbor and on second-nearest neighbor, marked as X on the schematic. We label our 112 triplets in XYX elemental order, i.e., the middle element is unique while the two outer elements are equivalent to each other, e.g., AlMgCu 112 = CuMgAl 112 != AlCuMg 112. These structures are included in the training set.

Figure 13 shows the predicted substitutional energies for the NNPs and obtained via DFT. Very good agreement is found for all of the different substitutions in the η'_{IV} (the lowest energy η' phase according to DFT) and the T phase. The only notable deviations arise for substitution of Cu by Mg, Mg →Cu, which is energetically the most unfavorable substitution and so will not arise physically. The error is thus unimportant for studying real alloys.

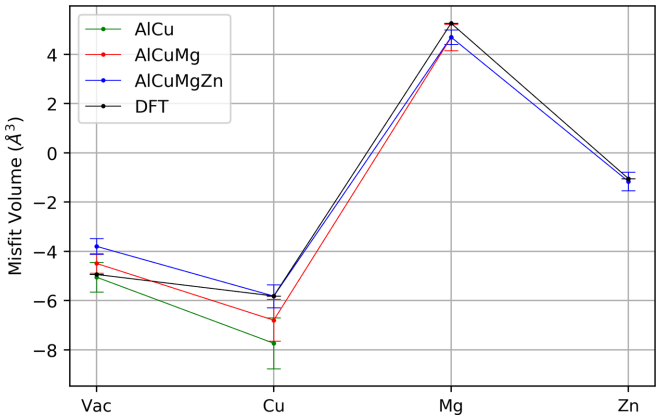

FIG. 10. Misfit volumes for the Vacancy and for Cu, Mg, and Zn solutes in an Al matrix, as predicted by DFT and the various NNPs as indicated. These structures are included in the training set.

IV. RESULTS: TRANSFERABILITY

A. Generalized stacking fault of the S phase

Here we examine the capability of the Al-Cu-Mg potential to predict the generalized stacking fault energy (GSFE) surface of the S phase on the relevant planes for shearing of S-phase precipitates in an Al matrix. Our structure for the S phase is the PW model [76] confirmed by Wolverton [77] and later Liu *et al.* [75]. It is an orthorhombic structure of the cmcm spacegroup, where we use our DFT-relaxed lattice vectors of a = 4.01, b = 9.27, and c = 7.14. We follow the same methodology as in our previous paper [2], including the usage of a short-range repulsive Lennard-Jones (LJ) term as we discuss in Ref. [4]. We briefly summarize the key details here.

First, we use the crystallographic methodology described by Cayron [78] and as implemented in the GenOVa program [79] along with the Al/S-phase orientation relationship (OR) to find the S-phase slip planes that are well-aligned with the {111} planes and $\frac{1}{2}\langle 112\rangle$ slip directions in FCC Al. Not all {111} Al planes are equivalent in the S phase. We find that there are two different families of slip planes in the S-phase: $\{\overline{1}12\}$ and $\{1\overline{3}1\}$. The normal vectors for these planes deviate from those of {111} Al by 3.81° and 4.15° respectively. We also show the results for the $\{\overline{3}37\}$ and $\{9\ \overline{2}8\ 7\}$ planes, have much smaller deviations of 0.87° and 0.23°, respectively, but are more complex.

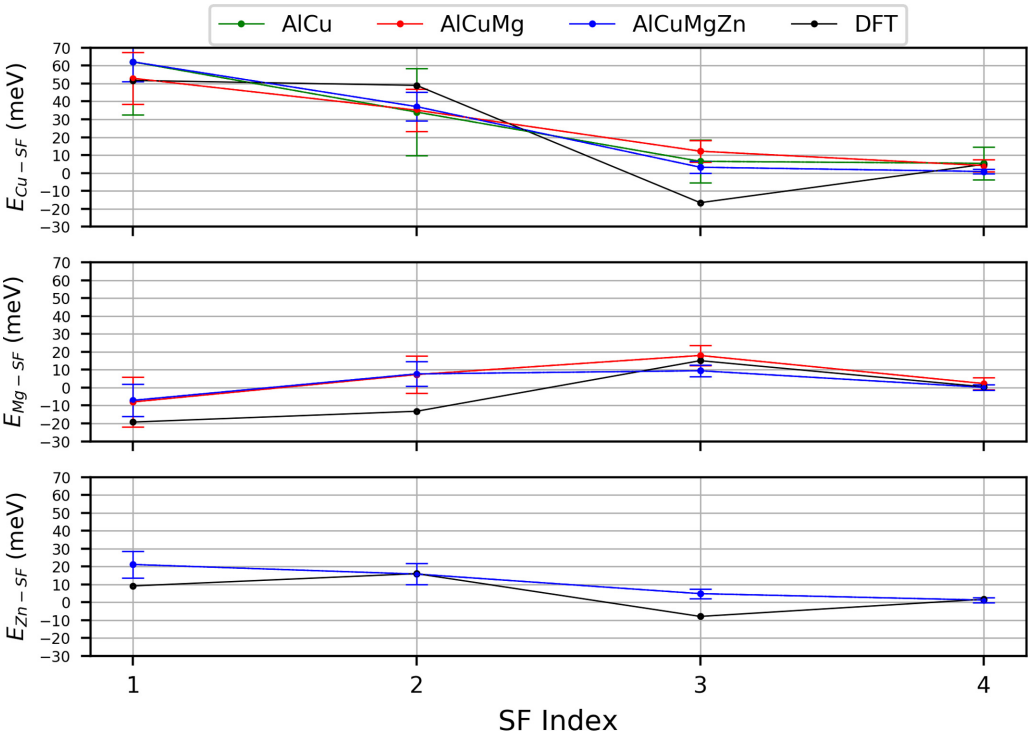

FIG. 11. Solute-stackingfault interaction energy for Cu, Mg, and Zn in Al matrix for the four sites closest to the stacking fault. These structures are included in the training set.

To compute the GSFE surface for the identified planes of interest, we follow the same general procedure as [4] and based on the methods developed in [80]. We start by constructing unit cells whose z axis is normal to the $\{\overline{1}12\}$ or $\{13\overline{1}\}$ planes of the S phase, resulting in a cell having some vectors a_1, a_2, a_3, where a_1 and a_2 span the plane of interest and a_3 is chosen to ensure periodicity. We note that the proper construction of such a cell is somewhat involved, and is discussed at great length in [4]. We then shift a_3 by in-plane vectors $\mathbf{t}$ to $a_3 + \mathbf{t}$, and relax both the atoms and the cell in the z direction only to obtain the fault energy at slip vector $\mathbf{t}$. During this procedure some configurations may arise where the atoms are highly overlapped and, being far outside the NNP training set, may cause a total collapse of the system. These configurations arise due to the procedure, and would not occur naturally, and hence to avoid the unphysical behavior we add the cut-and-shifted repulsive Lennard Jones potential that is zero over the range of physically-accessible lengths; numerical detail are given in Appendix I.

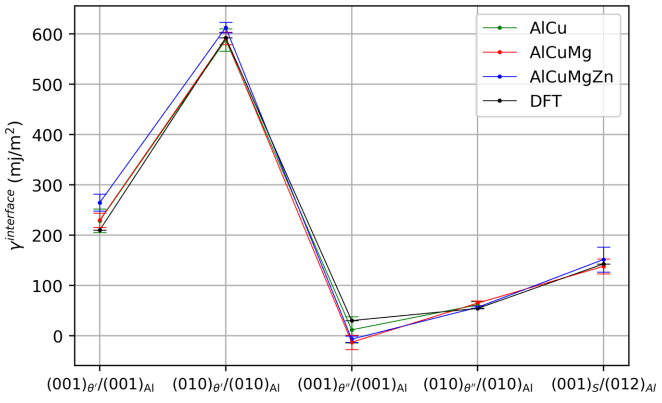

FIG. 12. Energy of S/Al interface as well as the semicoherent and coherent versions of θ and θ' interfaces for NNPs and DFT. These structures are included in the training set.

Figure 14 shows the atomic structure and GSFE surface for the S$(1\overline{3}1)$ and S$(\overline{1}12)$ surfaces, both of which are smooth. The S$(\overline{1}12)$ surface has lower energies than the S$(1\overline{3}1)$ surface over most of the domain, and so we predict that the precipitate will shear most readily on the S$(\overline{1}12)$ surface. Figure 14 also shows the positions of slip corresponding to the Al $\langle 111\rangle\{110\}$ Burgers vectors, and the energies at these locations correspond to the shearing energy for a matrix Al dislocation to shear the S-phase. These values for the S$(\overline{1}12)$ surface are indeed lower than those for the S$(1\overline{3}1)$ surface, further supporting the prediction that shearing will occur on the S$(\overline{1}12)$ planes.

Figure 15 validates the NNP results by comparing key points on the GSFE against a posteriori DFT calculations. The NNP predictions agree very well with the DFT results for all the different surfaces and Al Burgers vectors, deviating only by 100 mJ/m^2 with total energies being much larger. The NNP training did not include any structures corresponding to the GSFE surfaces, and so this result is a strong validation of the NNP for a critical feature controlling strengthening in Al-Cu-Mg alloys.

The misalignment of the S$(\overline{1}12)$ and S$(1\overline{3}1)$ surface relative to an Al matrix is not small, and so dislocation shearing would also result in a residual Burgers vector content with some energy cost. We thus examine the GSFEs for the well-aligned $\{\overline{3}37\}$ and $\{9\ \overline{2}8\ 7\}$ planes. These surfaces require very large

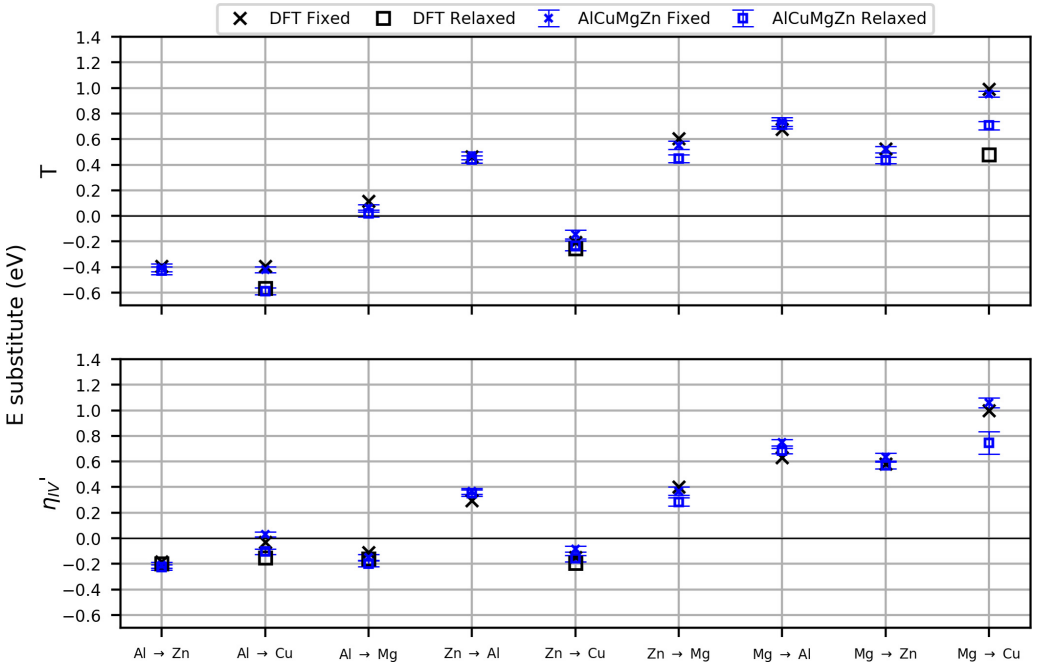

FIG. 13. DFT antisite formation energy vs NNP antisite formation energy for η' and T phases. These structures are included in the training set.

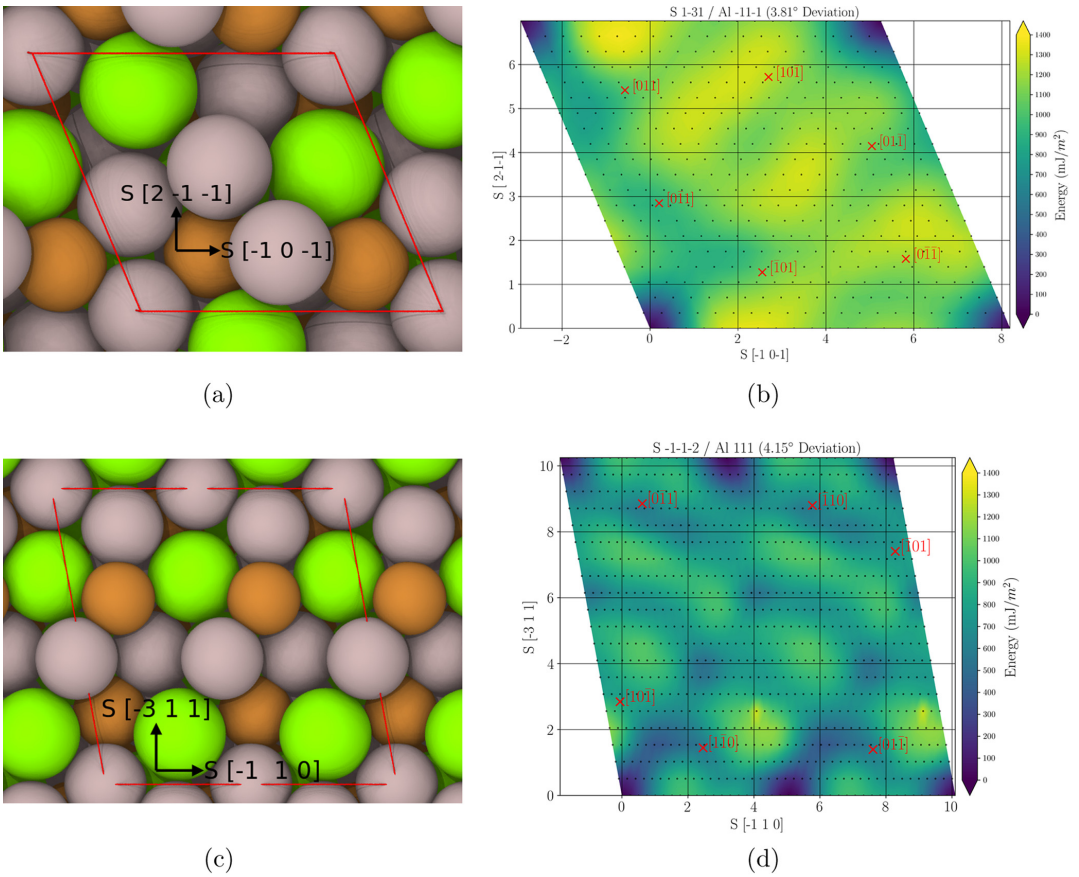

FIG. 14. Image of (a) the S($1\bar{3}1$) and (c) S($\overline{112}$) atomic surface structures and [(b),(d)] their corresponding GSFE surfaces. The ($\overline{112}$) surface is doubled in the S[$\bar{1}10$] direction for greater clarity of visualization. Grey atoms are Al, brown atoms are Cu, and green atoms are Mg. These structures are not included in the training set.

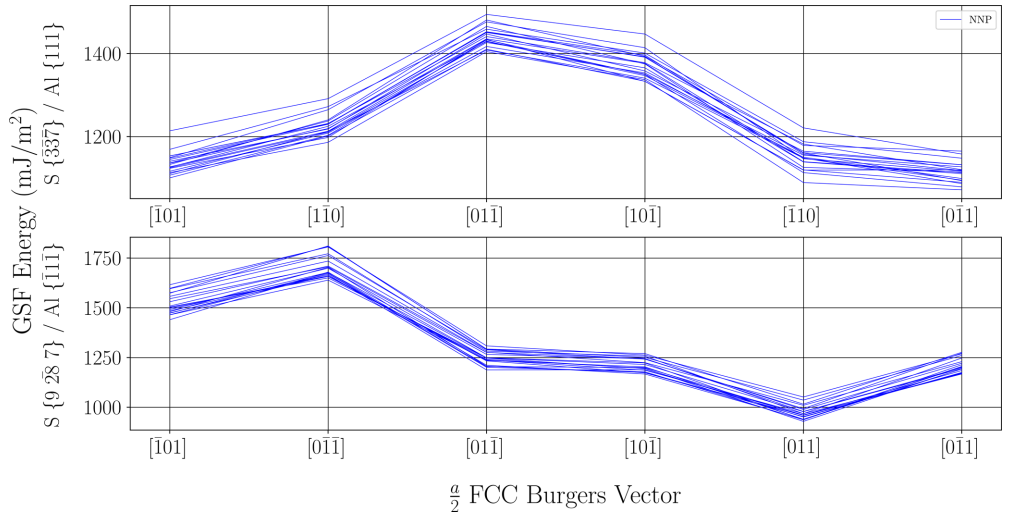

FIG. 15. Burgers vector vs GSFE using all AlCuMg NNPs for the S phase in the $\{9\ \overline{28}\ 7\}$ and $\{\overline{337}\}$ configurations. These results are computed with the LJ term. These structures are not included in the training set.

supercells that are not computationally tractable in DFT. We thus study only the predictions of the NNPs, as shown in Fig. 16. For these surfaces, the shearing energies are significantly higher than those for the S($\overline{112}$) plane, and the scatter among different NNPs is small. Thus, we expect that, in spite of the misalignment, the S($\overline{112}$) plane will be the dominant plane of shearing in the S phase.

B. AlZnMg clusters

Here we compare predictions of the AlCuMgZn NNPs to recent paper by Lervik *et al.* [29] on novel Mg-Zn clusters. The clusters are organized in four regions: a central, optional, interstitial element, followed by a Zn octahedron of 6 atoms, an Mg cube of 8 atoms, and finally a Zn truncated cube octahedron (TCO) of up to 24 atoms. These clusters are described with the notation $i\mathrm{M}_x\mathrm{Z}_y\mathrm{M}_z$ where $i = (a, m, z)$ (for Al, Mg, Zn), $x = (0, ..., 6)$, $y = (0, ...8)$ and $z = (0, ..., 24)$, e.g., $\mathrm{aZ_6M_8Z_{24}}$ is a cluster with an Aluminum interstitial, 6 Zn octahedral atoms, 8 Mg cube atoms, and 24 Zn TCO atoms; see Figs. 17(a)–17(d) for images of the inner shells. The formation energies are computed in the standard way, relative to solid solution energies. Here, we show both the energy per solute E_{form}/solute, which does not include Al atoms, and the total formation energy E_{form}/total of the cluster including the Al atoms. Figure 17(e) compares the predictions of the NNPs to the DFT results reported by Lervik *et al.* and to our own DFT results using settings consistent with the creation of the training set. Overall, the NNPs perform very well on all the different structures despite the absence of any such structures or any similar structures in the training set. The two DFT results differ slightly, and the NNP agrees better with our DFT, showing the importance of consistency in DFT methodology

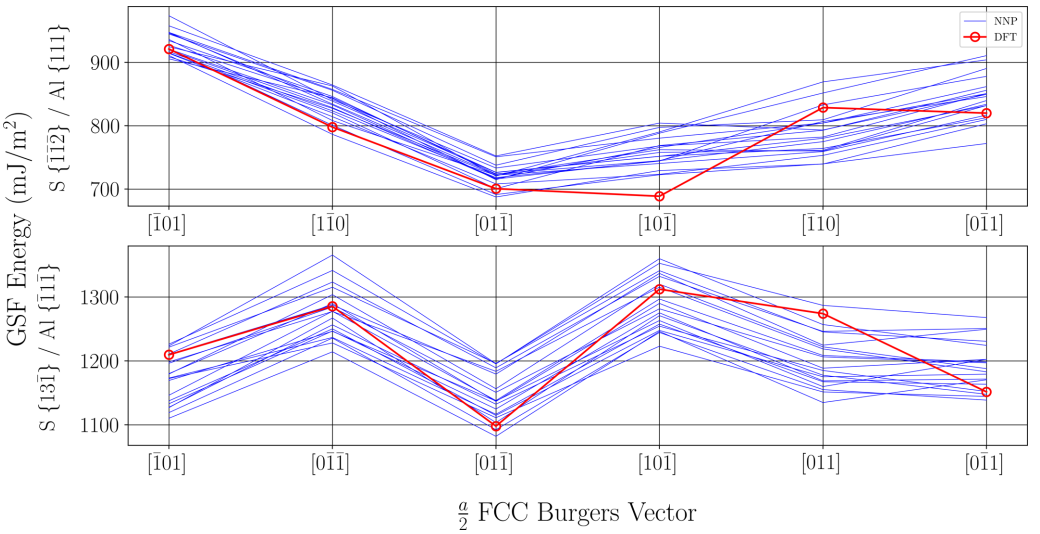

FIG. 16. Burgers vector vs GSFE using all AlCuMg NNPs and DFT for the S phase in the $\{1\bar{3}1\}$ and $\{\bar{1}1\bar{1}\}$ configurations. The NNPs show excellent ability to predict GSFEs for DFT with all DFT values being within, or near, the span of NNP-computed values. These results are computed with the LJ term. These structures are not included in the training set.

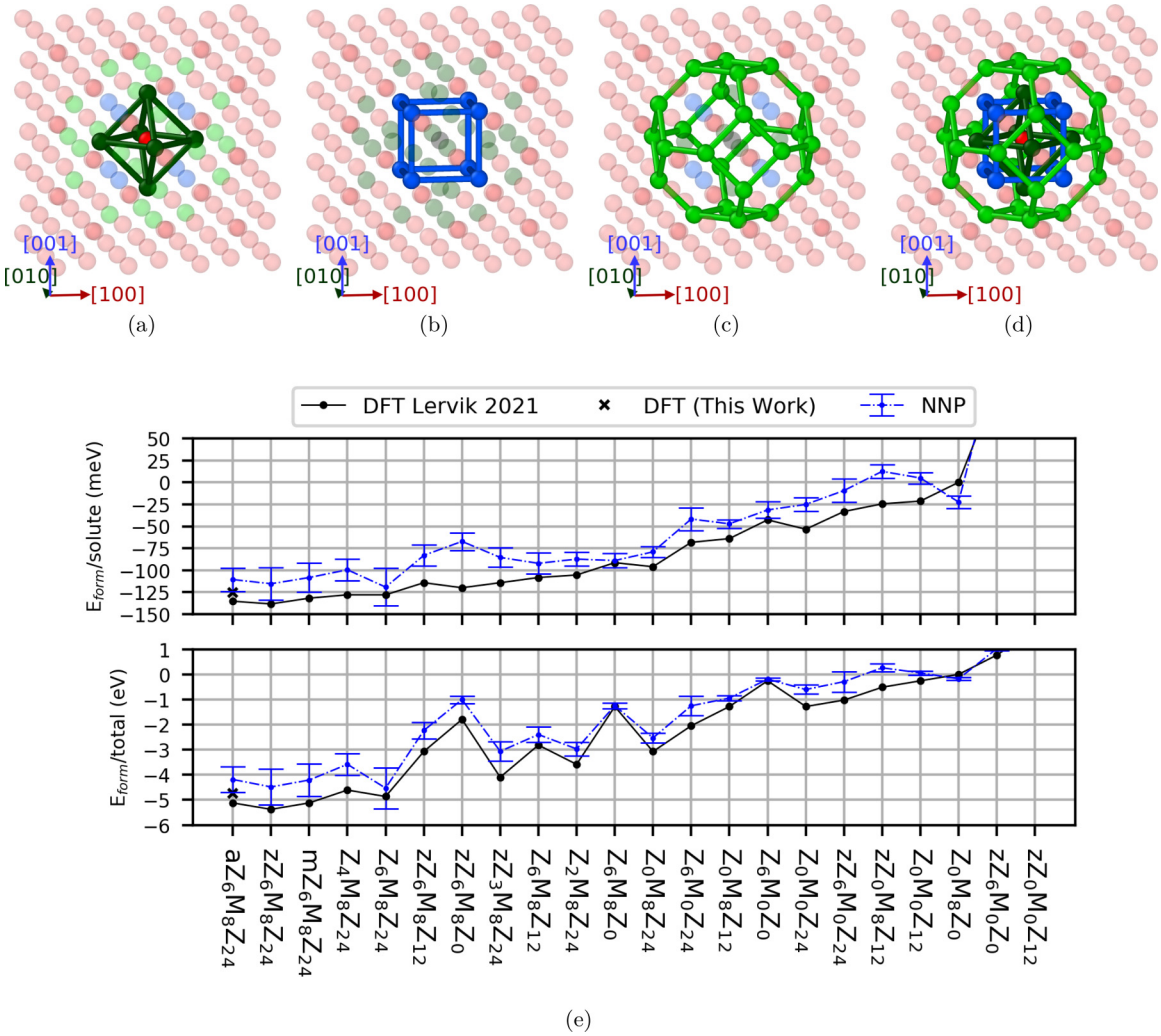

FIG. 17. [(a)–(d)] Images of solute sites, organized in shells, for Al-Zn-Mg cluster (a) interstitial site (dark red) and inner Zn octahedron (dark green) (b) Mg cube (c) Zn truncated cube octahedron (light green) (d) all shells and the interstitial. Miller indices are in reference to the Al matrix, whose atoms are light red and semi-transparent. See main text for a more detailed description. (e) Formation energies per solute (top) and for the entire structure (bottom) for Al-Zn-Mg clusters.

for creating and evaluating NNPs. The total cluster formation energies are also shown, and the agreement between the NNPs and DFT is again quite good.

C. Solute antisites, vacancies, and substitutions

We further validate the accuracy of the NNPs using the energetics of antisites and vacancies in Al-Cu-Mg ternary systems. Antisites and vacancies inevitably arise during the formation and growth of precipitates and so accuracy is important for any future thermodynamic/kinetic study. Here we use all the ternary Al-Cu-Mg structures in the OQMD database and compute these antisite and vacancy energies for every atom site using supercells of at least 108 atoms to minimize defect self-interactions in the periodic cell. We use the same means of computing formation energies, $\Delta E_f^{\text{antisite}}$, as for the T and η' phases as shown in Eq. (14), but do not relax the structure. The lack of relaxation is not important for our comparisons between the NNPs and DFT, but would be important in applications.

Figure 18 shows the antisite energies for ternary Al-Cu-Mg systems. Figure 32 of Appendix J shows antisite energies for binary Al-Cu. In cases where there are several unique sites for a given element we show only the site that has the lowest energy according to DFT, as this is the most important value to model correctly; otherwise the figure would be unreadable. Variations among the NNP energies are seen, but rarely exceed 0.1 eV, and the NNP average is close to the DFT value. The NNPs capture even small yet important differences in the antisites: e.g, that substituting Mg with Cu, Cu → Mg, in $Al_4Cu_{10}Mg_2$ is slightly negative. These results demonstrate that the NNPs make accurate predictions of point defects that are not in the training set. Referring to Appendix J, we see that despite the increased complexity of the Al-Cu-Mg dataset, the NNP yields very good results for antisites in Al-Cu, with results comparable to those found using a previous Al-Cu NNP [2].

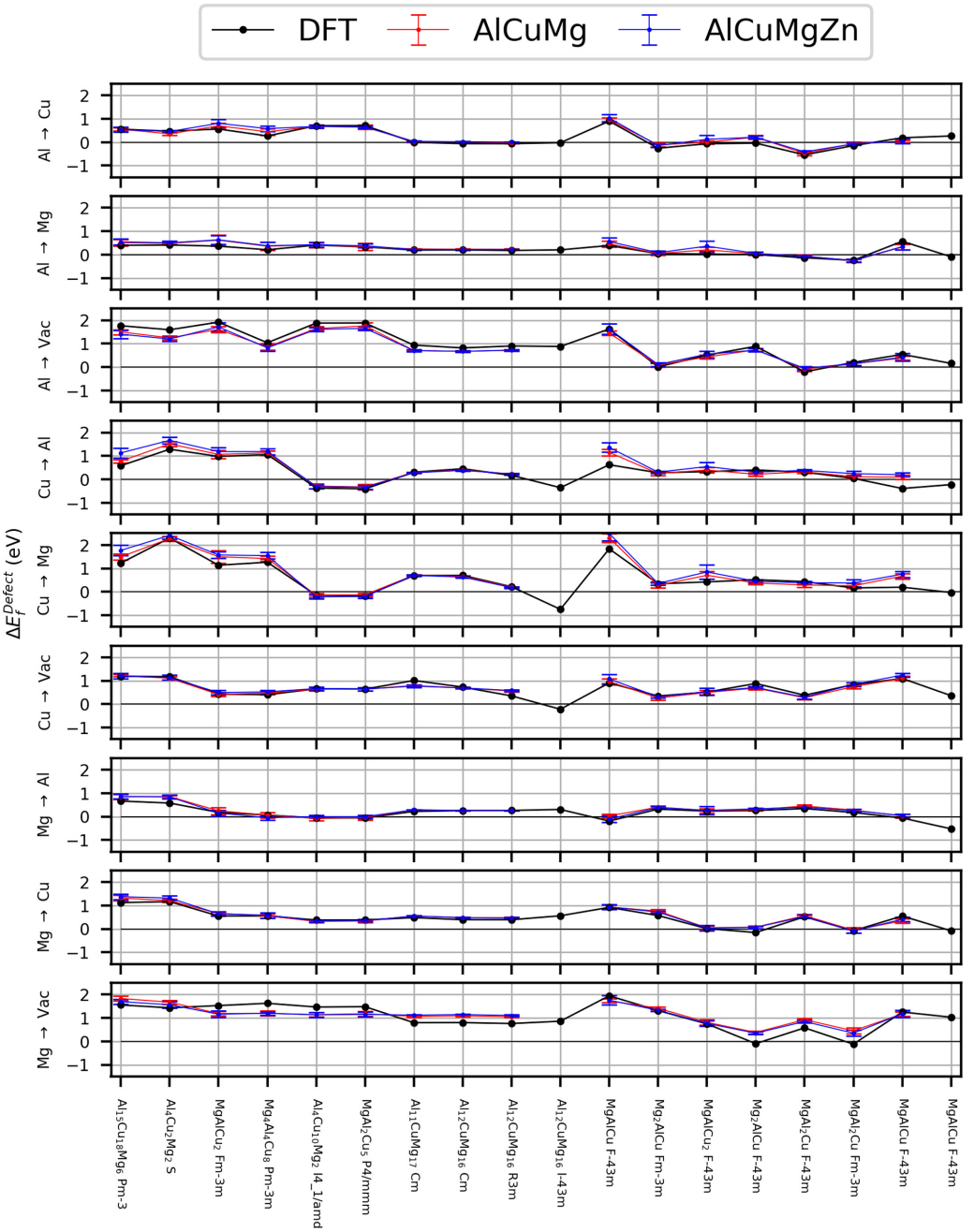

FIG. 18. DFT antisite formation energy vs NNP antisite formation energy for Al-Cu-Mg compounds. These structures are not included in the training set.

V. CONCLUSIONS

In this paper we have created and tested sets of near-DFT-accurate Al-Cu-Mg and Al-Cu-Mg-Zn potentials using the Behler-Parinello neural network formulation. We were able to achieve this state-of-the-art performance by extending our previous datasets involving Al-Cu and Al-Mg-Si to include new data pertinent to the Al-Cu-Mg-Zn alloys, and thus we continue to prove the viability of this methodology to construct high-quality metallurgical potentials. The NNPs reliably predicted essential alloy properties including lattice constants, elastic constants, surface and stacking fault energies, precipitate formation energies, and precipitate antisite or substitutional defects. We have demonstrated that these NNPs are able to accurately predict (within 100 mJ/m^2 of DFT) GSFE surface of the terminal S phase, thus making our potential the first, to our knowledge, able to accurately model dislocation-precipitate strengthening for this system. Finally our four-element potential for Al-Cu-Mg-Zn that shows very good predictions for (i) the role of Cu in aiding η' and T phase formation and (ii) novel Al-Zn-Mg clusters without explicit training.

The NNPs are not perfect and we find similar errors and issues as noted in our previous paper [2,4]. For example, C_{44} for Al remains challenging to model. Also, the NNPs are highly inaccurate at close-range interatomic distances requiring the addition of an ad-hoc repulsive potential to avoid unphysi-

cal behavior in this regime. There are clear paths that may improve these potentials, e.g., improvements in symmetry function selection, new types of symmetry functions, incorporating a loss function that considers energy differences, and/or new optimization techniques. However, in many key aspects the NNPs are very accurate and are the first potentials suitable for any realistic metallurgical modeling of Al-Cu-Mg-Zn.

We can anticipate that the methodology can be successfully extended into other alloying elements. At the same time, other machine learning methods combined with our training data may yield even better potentials. To this end, we provide all of our training data on the Materials Cloud [54] and invite the community to train or test other potentials or methods.

Broadly, however, our results here show that by using a sufficient dataset covering a wide range of metallurgically relevant structures, the computationally-efficient NNP formulation produces potentials with the accuracy needed for many metallurgical applications. This success is thus another demonstration of the value of the underlying approach and methodology, advancing the applications of machine learning interatomic potentials to realistic computational metallurgy.

ACKNOWLEDGMENTS

This research was supported by the NCCR MARVEL, a National Centre of Competence in Research, funded by the Swiss National Science Foundation (Grant No. 182892).

APPENDIX A: SYMMETRY FUNCTION HYPERPARAMETERS

In this section we show all the symmetry functions used for the neural network potentials.

TABLE I. Hyperparameters for the radial symmetry functions for Al-Cu-Mg NNPs.

Element1	Element2	η	r_2	r_c
Al	Al	1.000×10^{-2}	0.000×10^{0}	2.000×10^{1}
Al	Al	1.073×10^{-1}	0.000×10^{0}	2.000×10^{1}
Al	Al	1.117×10^{-1}	1.301×10^{1}	2.000×10^{1}
Al	Al	1.166×10^{-1}	7.071×10^{0}	2.000×10^{1}
Al	Al	1.350×10^{-1}	9.170×10^{0}	2.000×10^{1}
Al	Al	1.560×10^{-2}	0.000×10^{0}	2.000×10^{1}
Al	Al	1.689×10^{-1}	1.057×10^{1}	2.000×10^{1}
Al	Al	2.102×10^{-1}	0.000×10^{0}	2.000×10^{1}
Al	Al	2.109×10^{-1}	7.336×10^{0}	2.000×10^{1}
Al	Al	2.500×10^{-3}	0.000×10^{0}	2.000×10^{1}
Al	Al	2.982×10^{-1}	6.169×10^{0}	2.000×10^{1}
Al	Al	3.580×10^{-2}	0.000×10^{0}	2.000×10^{1}
Al	Al	3.900×10^{-3}	0.000×10^{0}	2.000×10^{1}
Al	Al	4.466×10^{-1}	6.504×10^{0}	2.000×10^{1}
Al	Al	4.770×10^{-2}	1.542×10^{1}	2.000×10^{1}
Al	Al	5.830×10^{-2}	1.000×10^{1}	2.000×10^{1}
Al	Al	6.900×10^{-3}	0.000×10^{0}	2.000×10^{1}
Al	Al	7.460×10^{-2}	1.234×10^{1}	2.000×10^{1}
Al	Al	8.020×10^{-2}	1.189×10^{1}	2.000×10^{1}
Al	Cu	1.073×10^{-1}	0.000×10^{0}	1.600×10^{1}
Al	Cu	1.117×10^{-1}	1.301×10^{1}	1.600×10^{1}
Al	Cu	1.166×10^{-1}	7.071×10^{0}	2.000×10^{1}
Al	Cu	1.350×10^{-1}	9.170×10^{0}	2.000×10^{1}
Al	Cu	1.560×10^{-2}	0.000×10^{0}	8.000×10^{0}
Al	Cu	1.689×10^{-1}	1.057×10^{1}	1.600×10^{1}
Al	Cu	2.102×10^{-1}	0.000×10^{0}	8.000×10^{0}
Al	Cu	2.109×10^{-1}	7.336×10^{0}	1.600×10^{1}
Al	Cu	2.500×10^{-3}	0.000×10^{0}	2.000×10^{1}
Al	Cu	2.982×10^{-1}	6.169×10^{0}	8.000×10^{0}
Al	Cu	3.900×10^{-3}	0.000×10^{0}	1.600×10^{1}
Al	Cu	4.466×10^{-1}	6.504×10^{0}	8.000×10^{0}
Al	Cu	4.770×10^{-2}	1.542×10^{1}	2.000×10^{1}
Al	Cu	5.830×10^{-2}	1.000×10^{1}	2.000×10^{1}
Al	Cu	6.900×10^{-3}	0.000×10^{0}	1.200×10^{1}
Al	Cu	7.100×10^{-3}	0.000×10^{0}	2.000×10^{1}
Al	Cu	7.460×10^{-2}	1.234×10^{1}	1.600×10^{1}
Al	Cu	8.020×10^{-2}	1.189×10^{1}	2.000×10^{1}
Al	Mg	1.000×10^{-2}	0.000×10^{0}	2.000×10^{1}
Al	Mg	1.073×10^{-1}	0.000×10^{0}	1.600×10^{1}
Al	Mg	1.117×10^{-1}	1.301×10^{1}	1.600×10^{1}
Al	Mg	1.166×10^{-1}	7.071×10^{0}	2.000×10^{1}
Al	Mg	1.350×10^{-1}	9.170×10^{0}	2.000×10^{1}
Al	Mg	1.560×10^{-2}	0.000×10^{0}	8.000×10^{0}
Al	Mg	1.689×10^{-1}	1.057×10^{1}	1.600×10^{1}
Al	Mg	1.875×10^{-1}	0.000×10^{0}	8.000×10^{0}
Al	Mg	2.109×10^{-1}	7.336×10^{0}	1.600×10^{1}
Al	Mg	2.500×10^{-3}	0.000×10^{0}	2.000×10^{1}
Al	Mg	2.982×10^{-1}	6.169×10^{0}	8.000×10^{0}
Al	Mg	3.900×10^{-3}	0.000×10^{0}	1.600×10^{1}
Al	Mg	4.466×10^{-1}	6.504×10^{0}	8.000×10^{0}
Al	Mg	4.770×10^{-2}	1.542×10^{1}	2.000×10^{1}
Al	Mg	5.830×10^{-2}	1.000×10^{1}	2.000×10^{1}
Al	Mg	6.900×10^{-3}	0.000×10^{0}	1.200×10^{1}
Al	Mg	7.460×10^{-2}	1.234×10^{1}	1.600×10^{1}
Al	Mg	8.020×10^{-2}	1.189×10^{1}	2.000×10^{1}
Cu	Al	1.000×10^{-2}	0.000×10^{0}	2.000×10^{1}
Cu	Al	1.073×10^{-1}	0.000×10^{0}	1.600×10^{1}
Cu	Al	1.117×10^{-1}	1.301×10^{1}	1.600×10^{1}
Cu	Al	1.166×10^{-1}	7.071×10^{0}	2.000×10^{1}
Cu	Al	1.350×10^{-1}	9.170×10^{0}	2.000×10^{1}
Cu	Al	1.560×10^{-2}	0.000×10^{0}	8.000×10^{0}
Cu	Al	1.689×10^{-1}	1.057×10^{1}	1.600×10^{1}
Cu	Al	1.875×10^{-1}	0.000×10^{0}	8.000×10^{0}
Cu	Al	2.109×10^{-1}	7.336×10^{0}	1.600×10^{1}
Cu	Al	2.500×10^{-3}	0.000×10^{0}	2.000×10^{1}
Cu	Al	2.982×10^{-1}	6.169×10^{0}	8.000×10^{0}
Cu	Al	3.900×10^{-3}	0.000×10^{0}	1.600×10^{1}
Cu	Al	4.466×10^{-1}	6.504×10^{0}	8.000×10^{0}
Cu	Al	4.770×10^{-2}	1.542×10^{1}	2.000×10^{1}
Cu	Al	5.830×10^{-2}	1.000×10^{1}	2.000×10^{1}
Cu	Al	6.900×10^{-3}	0.000×10^{0}	1.200×10^{1}
Cu	Al	7.460×10^{-2}	1.234×10^{1}	1.600×10^{1}
Cu	Al	8.020×10^{-2}	1.189×10^{1}	2.000×10^{1}
Cu	Cu	1.000×10^{-2}	0.000×10^{0}	2.000×10^{1}
Cu	Cu	1.073×10^{-1}	0.000×10^{0}	1.600×10^{1}
Cu	Cu	1.117×10^{-1}	1.301×10^{1}	1.600×10^{1}
Cu	Cu	1.166×10^{-1}	7.071×10^{0}	2.000×10^{1}
Cu	Cu	1.350×10^{-1}	9.170×10^{0}	2.000×10^{1}
Cu	Cu	1.560×10^{-2}	0.000×10^{0}	8.000×10^{0}
Cu	Cu	1.590×10^{-2}	0.000×10^{0}	1.200×10^{1}
Cu	Cu	1.689×10^{-1}	1.057×10^{1}	1.600×10^{1}

TABLE I. (*Continued.*)

Element1	Element2	η	r_2	r_c
Cu	Cu	2.102×10^{-1}	0.000×10^{0}	8.000×10^{0}
Cu	Cu	2.109×10^{-1}	7.336×10^{0}	1.600×10^{1}
Cu	Cu	2.500×10^{-3}	0.000×10^{0}	2.000×10^{1}
Cu	Cu	2.982×10^{-1}	6.169×10^{0}	8.000×10^{0}
Cu	Cu	3.580×10^{-2}	0.000×10^{0}	8.000×10^{0}
Cu	Cu	3.900×10^{-3}	0.000×10^{0}	1.600×10^{1}
Cu	Cu	4.466×10^{-1}	6.504×10^{0}	8.000×10^{0}
Cu	Cu	4.770×10^{-2}	1.542×10^{1}	2.000×10^{1}
Cu	Cu	5.830×10^{-2}	1.000×10^{1}	2.000×10^{1}
Cu	Cu	6.900×10^{-3}	0.000×10^{0}	1.200×10^{1}
Cu	Cu	7.460×10^{-2}	1.234×10^{1}	1.600×10^{1}
Cu	Cu	8.020×10^{-2}	1.189×10^{1}	2.000×10^{1}
Cu	Mg	1.000×10^{-2}	0.000×10^{0}	2.000×10^{1}
Cu	Mg	1.073×10^{-1}	0.000×10^{0}	1.600×10^{1}
Cu	Mg	1.117×10^{-1}	1.301×10^{1}	1.600×10^{1}
Cu	Mg	1.166×10^{-1}	7.071×10^{0}	2.000×10^{1}
Cu	Mg	1.350×10^{-1}	9.170×10^{0}	2.000×10^{1}
Cu	Mg	1.560×10^{-2}	0.000×10^{0}	8.000×10^{0}
Cu	Mg	1.689×10^{-1}	1.057×10^{1}	1.600×10^{1}
Cu	Mg	2.109×10^{-1}	7.336×10^{0}	1.600×10^{1}
Cu	Mg	2.500×10^{-3}	0.000×10^{0}	2.000×10^{1}
Cu	Mg	2.982×10^{-1}	6.169×10^{0}	8.000×10^{0}
Cu	Mg	3.900×10^{-3}	0.000×10^{0}	1.600×10^{1}
Cu	Mg	4.466×10^{-1}	6.504×10^{0}	8.000×10^{0}
Cu	Mg	4.770×10^{-2}	1.542×10^{1}	2.000×10^{1}
Cu	Mg	5.830×10^{-2}	1.000×10^{1}	2.000×10^{1}
Cu	Mg	6.900×10^{-3}	0.000×10^{0}	1.200×10^{1}
Cu	Mg	7.460×10^{-2}	1.234×10^{1}	1.600×10^{1}
Cu	Mg	8.020×10^{-2}	1.189×10^{1}	2.000×10^{1}
Mg	Al	1.000×10^{-2}	0.000×10^{0}	2.000×10^{1}
Mg	Al	1.073×10^{-1}	0.000×10^{0}	1.600×10^{1}
Mg	Al	1.117×10^{-1}	1.301×10^{1}	1.600×10^{1}
Mg	Al	1.166×10^{-1}	7.071×10^{0}	2.000×10^{1}
Mg	Al	1.350×10^{-1}	9.170×10^{0}	2.000×10^{1}
Mg	Al	1.560×10^{-2}	0.000×10^{0}	8.000×10^{0}
Mg	Al	1.689×10^{-1}	1.057×10^{1}	1.600×10^{1}
Mg	Al	2.102×10^{-1}	0.000×10^{0}	8.000×10^{0}
Mg	Al	2.109×10^{-1}	7.336×10^{0}	1.600×10^{1}
Mg	Al	2.500×10^{-3}	0.000×10^{0}	2.000×10^{1}
Mg	Al	2.982×10^{-1}	6.169×10^{0}	8.000×10^{0}
Mg	Al	3.580×10^{-2}	0.000×10^{0}	8.000×10^{0}
Mg	Al	3.900×10^{-3}	0.000×10^{0}	1.600×10^{1}
Mg	Al	4.466×10^{-1}	6.504×10^{0}	8.000×10^{0}

TABLE I. (*Continued.*)

Element1	Element2	η	r_2	r_c
Mg	Al	4.770×10^{-2}	1.542×10^{1}	2.000×10^{1}
Mg	Al	5.830×10^{-2}	1.000×10^{1}	2.000×10^{1}
Mg	Al	6.900×10^{-3}	0.000×10^{0}	1.200×10^{1}
Mg	Al	7.460×10^{-2}	1.234×10^{1}	1.600×10^{1}
Mg	Al	8.020×10^{-2}	1.189×10^{1}	2.000×10^{1}
Mg	Cu	1.000×10^{-2}	0.000×10^{0}	2.000×10^{1}
Mg	Cu	1.073×10^{-1}	0.000×10^{0}	1.600×10^{1}
Mg	Cu	1.117×10^{-1}	1.301×10^{1}	1.600×10^{1}
Mg	Cu	1.166×10^{-1}	7.071×10^{0}	2.000×10^{1}
Mg	Cu	1.350×10^{-1}	9.170×10^{0}	2.000×10^{1}
Mg	Cu	1.560×10^{-2}	0.000×10^{0}	8.000×10^{0}
Mg	Cu	1.689×10^{-1}	1.057×10^{1}	1.600×10^{1}
Mg	Cu	2.109×10^{-1}	7.336×10^{0}	1.600×10^{1}
Mg	Cu	2.500×10^{-3}	0.000×10^{0}	2.000×10^{1}
Mg	Cu	2.982×10^{-1}	6.169×10^{0}	8.000×10^{0}
Mg	Cu	3.580×10^{-2}	0.000×10^{0}	8.000×10^{0}
Mg	Cu	3.900×10^{-3}	0.000×10^{0}	1.600×10^{1}
Mg	Cu	4.466×10^{-1}	6.504×10^{0}	8.000×10^{0}
Mg	Cu	4.770×10^{-2}	1.542×10^{1}	2.000×10^{1}
Mg	Cu	5.830×10^{-2}	1.000×10^{1}	2.000×10^{1}
Mg	Cu	6.900×10^{-3}	0.000×10^{0}	1.200×10^{1}
Mg	Cu	7.460×10^{-2}	1.234×10^{1}	1.600×10^{1}
Mg	Cu	8.020×10^{-2}	1.189×10^{1}	2.000×10^{1}
Mg	Mg	1.000×10^{-2}	0.000×10^{0}	2.000×10^{1}
Mg	Mg	1.073×10^{-1}	0.000×10^{0}	1.600×10^{1}
Mg	Mg	1.117×10^{-1}	1.301×10^{1}	1.600×10^{1}
Mg	Mg	1.166×10^{-1}	7.071×10^{0}	2.000×10^{1}
Mg	Mg	1.350×10^{-1}	9.170×10^{0}	2.000×10^{1}
Mg	Mg	1.560×10^{-2}	0.000×10^{0}	8.000×10^{0}
Mg	Mg	1.689×10^{-1}	1.057×10^{1}	1.600×10^{1}
Mg	Mg	2.109×10^{-1}	7.336×10^{0}	1.600×10^{1}
Mg	Mg	2.500×10^{-3}	0.000×10^{0}	2.000×10^{1}
Mg	Mg	2.982×10^{-1}	6.169×10^{0}	8.000×10^{0}
Mg	Mg	3.580×10^{-2}	0.000×10^{0}	8.000×10^{0}
Mg	Mg	3.900×10^{-3}	0.000×10^{0}	1.600×10^{1}
Mg	Mg	4.466×10^{-1}	6.504×10^{0}	8.000×10^{0}
Mg	Mg	4.770×10^{-2}	1.542×10^{1}	2.000×10^{1}
Mg	Mg	5.660×10^{-2}	0.000×10^{0}	2.000×10^{1}
Mg	Mg	5.830×10^{-2}	1.000×10^{1}	2.000×10^{1}
Mg	Mg	6.900×10^{-3}	0.000×10^{0}	1.200×10^{1}
Mg	Mg	7.460×10^{-2}	1.234×10^{1}	1.600×10^{1}
Mg	Mg	8.020×10^{-2}	1.189×10^{1}	2.000×10^{1}

TABLE II. Hyperparameters for the angular symmetry functions added by CURSEL for Al-Cu-Mg NNPs.

Element1	Element2	Element3	η	λ	ζ	r_c
Al	Al	Al	3.900×10^{-3}	-1	1.0	2.000×10^{1}
Al	Al	Al	3.900×10^{-3}	1	1.0	2.000×10^{1}
Al	Al	Al	8.900×10^{-3}	1	1.0	2.000×10^{1}
Al	Al	Cu	1.350×10^{-2}	1	1.0	1.600×10^{1}
Al	Al	Cu	3.900×10^{-3}	-1	1.0	1.600×10^{1}
Al	Al	Cu	3.900×10^{-3}	1	1.0	1.600×10^{1}
Al	Cu	Cu	3.900×10^{-3}	1	1.0	1.600×10^{1}
Al	Mg	Al	3.900×10^{-3}	1	1.0	1.600×10^{1}
Al	Mg	Cu	3.900×10^{-3}	1	1.0	1.600×10^{1}
Cu	Al	Al	3.900×10^{-3}	1	1.0	1.600×10^{1}
Cu	Al	Cu	1.350×10^{-2}	1	1.0	1.600×10^{1}
Cu	Al	Cu	3.900×10^{-3}	-1	1.0	1.600×10^{1}
Cu	Al	Cu	3.900×10^{-3}	1	1.0	1.600×10^{1}
Cu	Cu	Cu	3.900×10^{-3}	1	1.0	1.600×10^{1}
Cu	Mg	Al	3.900×10^{-3}	1	1.0	1.600×10^{1}
Cu	Mg	Cu	3.900×10^{-3}	-1	1.0	1.600×10^{1}
Cu	Mg	Cu	3.900×10^{-3}	1	1.0	1.600×10^{1}
Cu	Mg	Mg	3.900×10^{-3}	1	1.0	1.600×10^{1}
Mg	Al	Al	3.900×10^{-3}	1	1.0	1.600×10^{1}
Mg	Al	Cu	3.900×10^{-3}	1	1.0	1.600×10^{1}
Mg	Cu	Cu	3.900×10^{-3}	1	1.0	1.600×10^{1}
Mg	Mg	Al	3.900×10^{-3}	-1	1.0	1.600×10^{1}
Mg	Mg	Al	3.900×10^{-3}	1	1.0	1.600×10^{1}
Mg	Mg	Cu	3.900×10^{-3}	-1	1.0	1.600×10^{1}
Mg	Mg	Cu	3.900×10^{-3}	1	1.0	1.600×10^{1}
Mg	Mg	Mg	3.900×10^{-3}	1	1.0	1.600×10^{1}

TABLE III. Hyperparameters for the radial symmetry functions for Al-Cu-Mg-Zn NNPs.

Element1	Element2	η	r_2	r_c
Al	Al	1.117×10^{-1}	1.301×10^{1}	1.600×10^{1}
Al	Al	1.166×10^{-1}	7.071×10^{0}	2.000×10^{1}
Al	Al	1.350×10^{-1}	9.170×10^{0}	2.000×10^{1}
Al	Al	1.560×10^{-2}	0.000×10^{0}	8.000×10^{0}
Al	Al	1.590×10^{-2}	0.000×10^{0}	1.200×10^{1}
Al	Al	1.600×10^{-1}	0.000×10^{0}	2.000×10^{1}
Al	Al	1.689×10^{-1}	1.057×10^{1}	1.600×10^{1}
Al	Al	2.102×10^{-1}	0.000×10^{0}	8.000×10^{0}
Al	Al	2.109×10^{-1}	7.336×10^{0}	1.600×10^{1}
Al	Al	2.500×10^{-3}	0.000×10^{0}	2.000×10^{1}
Al	Al	2.982×10^{-1}	6.169×10^{0}	8.000×10^{0}
Al	Al	3.900×10^{-3}	0.000×10^{0}	1.600×10^{1}
Al	Al	4.466×10^{-1}	6.504×10^{0}	8.000×10^{0}
Al	Al	4.690×10^{-2}	0.000×10^{0}	1.600×10^{1}
Al	Al	4.770×10^{-2}	1.542×10^{1}	2.000×10^{1}
Al	Al	5.410×10^{-2}	0.000×10^{0}	8.000×10^{0}
Al	Al	5.830×10^{-2}	1.000×10^{1}	2.000×10^{1}
Al	Al	6.900×10^{-3}	0.000×10^{0}	1.200×10^{1}
Al	Al	7.100×10^{-3}	0.000×10^{0}	2.000×10^{1}

TABLE III. (*Continued.*)

Element1	Element2	η	r_2	r_c
Al	Al	7.460×10^{-2}	1.234×10^{1}	1.600×10^{1}
Al	Al	8.020×10^{-2}	1.189×10^{1}	2.000×10^{1}
Al	Cu	1.000×10^{-2}	0.000×10^{0}	2.000×10^{1}
Al	Cu	1.073×10^{-1}	0.000×10^{0}	1.600×10^{1}
Al	Cu	1.117×10^{-1}	1.301×10^{1}	1.600×10^{1}
Al	Cu	1.166×10^{-1}	7.071×10^{0}	2.000×10^{1}
Al	Cu	1.350×10^{-1}	9.170×10^{0}	2.000×10^{1}
Al	Cu	1.560×10^{-2}	0.000×10^{0}	8.000×10^{0}
Al	Cu	1.689×10^{-1}	1.057×10^{1}	1.600×10^{1}
Al	Cu	2.102×10^{-1}	0.000×10^{0}	8.000×10^{0}
Al	Cu	2.109×10^{-1}	7.336×10^{0}	1.600×10^{1}
Al	Cu	2.500×10^{-3}	0.000×10^{0}	2.000×10^{1}
Al	Cu	2.982×10^{-1}	6.169×10^{0}	8.000×10^{0}
Al	Cu	3.536×10^{-1}	0.000×10^{0}	8.000×10^{0}
Al	Cu	3.580×10^{-2}	0.000×10^{0}	8.000×10^{0}
Al	Cu	3.900×10^{-3}	0.000×10^{0}	1.600×10^{1}
Al	Cu	4.466×10^{-1}	6.504×10^{0}	8.000×10^{0}
Al	Cu	4.770×10^{-2}	1.542×10^{1}	2.000×10^{1}
Al	Cu	5.830×10^{-2}	1.000×10^{1}	2.000×10^{1}
Al	Cu	6.900×10^{-3}	0.000×10^{0}	1.200×10^{1}
Al	Cu	7.460×10^{-2}	1.234×10^{1}	1.600×10^{1}
Al	Cu	8.020×10^{-2}	1.189×10^{1}	2.000×10^{1}
Al	Mg	1.000×10^{-2}	0.000×10^{0}	2.000×10^{1}
Al	Mg	1.073×10^{-1}	0.000×10^{0}	1.600×10^{1}
Al	Mg	1.117×10^{-1}	1.301×10^{1}	1.600×10^{1}
Al	Mg	1.166×10^{-1}	7.071×10^{0}	2.000×10^{1}
Al	Mg	1.350×10^{-1}	9.170×10^{0}	2.000×10^{1}
Al	Mg	1.560×10^{-2}	0.000×10^{0}	8.000×10^{0}
Al	Mg	1.689×10^{-1}	1.057×10^{1}	1.600×10^{1}
Al	Mg	2.102×10^{-1}	0.000×10^{0}	8.000×10^{0}
Al	Mg	2.109×10^{-1}	7.336×10^{0}	1.600×10^{1}
Al	Mg	2.500×10^{-3}	0.000×10^{0}	2.000×10^{1}
Al	Mg	2.982×10^{-1}	6.169×10^{0}	8.000×10^{0}
Al	Mg	3.580×10^{-2}	0.000×10^{0}	8.000×10^{0}
Al	Mg	3.900×10^{-3}	0.000×10^{0}	1.600×10^{1}
Al	Mg	4.466×10^{-1}	6.504×10^{0}	8.000×10^{0}
Al	Mg	4.770×10^{-2}	1.542×10^{1}	2.000×10^{1}
Al	Mg	5.830×10^{-2}	1.000×10^{1}	2.000×10^{1}
Al	Mg	6.900×10^{-3}	0.000×10^{0}	1.200×10^{1}
Al	Mg	7.460×10^{-2}	1.234×10^{1}	1.600×10^{1}
Al	Mg	8.020×10^{-2}	1.189×10^{1}	2.000×10^{1}
Al	Zn	1.000×10^{-2}	0.000×10^{0}	2.000×10^{1}
Al	Zn	1.073×10^{-1}	0.000×10^{0}	1.600×10^{1}
Al	Zn	1.117×10^{-1}	1.301×10^{1}	1.600×10^{1}
Al	Zn	1.166×10^{-1}	7.071×10^{0}	2.000×10^{1}
Al	Zn	1.350×10^{-1}	9.170×10^{0}	2.000×10^{1}
Al	Zn	1.560×10^{-2}	0.000×10^{0}	8.000×10^{0}
Al	Zn	1.689×10^{-1}	1.057×10^{1}	1.600×10^{1}
Al	Zn	2.102×10^{-1}	0.000×10^{0}	8.000×10^{0}
Al	Zn	2.109×10^{-1}	7.336×10^{0}	1.600×10^{1}
Al	Zn	2.500×10^{-3}	0.000×10^{0}	2.000×10^{1}
Al	Zn	2.982×10^{-1}	6.169×10^{0}	8.000×10^{0}
Al	Zn	3.900×10^{-3}	0.000×10^{0}	1.600×10^{1}
Al	Zn	4.466×10^{-1}	6.504×10^{0}	8.000×10^{0}

TABLE III. (*Continued.*)

Element1	Element2	η	r_2	r_c
Al	Zn	4.770×10^{-2}	1.542×10^{1}	2.000×10^{1}
Al	Zn	5.830×10^{-2}	1.000×10^{1}	2.000×10^{1}
Al	Zn	6.900×10^{-3}	0.000×10^{0}	1.200×10^{1}
Al	Zn	7.460×10^{-2}	1.234×10^{1}	1.600×10^{1}
Al	Zn	8.020×10^{-2}	1.189×10^{1}	2.000×10^{1}
Cu	Al	1.000×10^{-2}	0.000×10^{0}	2.000×10^{1}
Cu	Al	1.117×10^{-1}	1.301×10^{1}	1.600×10^{1}
Cu	Al	1.166×10^{-1}	7.071×10^{0}	2.000×10^{1}
Cu	Al	1.350×10^{-1}	9.170×10^{0}	2.000×10^{1}
Cu	Al	1.560×10^{-2}	0.000×10^{0}	8.000×10^{0}
Cu	Al	1.600×10^{-1}	0.000×10^{0}	2.000×10^{1}
Cu	Al	1.689×10^{-1}	1.057×10^{1}	1.600×10^{1}
Cu	Al	2.102×10^{-1}	0.000×10^{0}	8.000×10^{0}
Cu	Al	2.109×10^{-1}	7.336×10^{0}	1.600×10^{1}
Cu	Al	2.500×10^{-3}	0.000×10^{0}	2.000×10^{1}
Cu	Al	2.982×10^{-1}	6.169×10^{0}	8.000×10^{0}
Cu	Al	3.900×10^{-3}	0.000×10^{0}	1.600×10^{1}
Cu	Al	4.466×10^{-1}	6.504×10^{0}	8.000×10^{0}
Cu	Al	4.770×10^{-2}	1.542×10^{1}	2.000×10^{1}
Cu	Al	5.830×10^{-2}	1.000×10^{1}	2.000×10^{1}
Cu	Al	6.900×10^{-3}	0.000×10^{0}	1.200×10^{1}
Cu	Al	7.460×10^{-2}	1.234×10^{1}	1.600×10^{1}
Cu	Al	8.020×10^{-2}	1.189×10^{1}	2.000×10^{1}
Cu	Cu	1.000×10^{-2}	0.000×10^{0}	2.000×10^{1}
Cu	Cu	1.117×10^{-1}	1.301×10^{1}	1.600×10^{1}
Cu	Cu	1.166×10^{-1}	7.071×10^{0}	2.000×10^{1}
Cu	Cu	1.350×10^{-1}	9.170×10^{0}	2.000×10^{1}
Cu	Cu	1.560×10^{-2}	0.000×10^{0}	8.000×10^{0}
Cu	Cu	1.590×10^{-2}	0.000×10^{0}	1.200×10^{1}
Cu	Cu	1.600×10^{-1}	0.000×10^{0}	2.000×10^{1}
Cu	Cu	1.689×10^{-1}	1.057×10^{1}	1.600×10^{1}
Cu	Cu	2.102×10^{-1}	0.000×10^{0}	8.000×10^{0}
Cu	Cu	2.109×10^{-1}	7.336×10^{0}	1.600×10^{1}
Cu	Cu	2.500×10^{-3}	0.000×10^{0}	2.000×10^{1}
Cu	Cu	2.982×10^{-1}	6.169×10^{0}	8.000×10^{0}
Cu	Cu	3.580×10^{-2}	0.000×10^{0}	8.000×10^{0}
Cu	Cu	3.900×10^{-3}	0.000×10^{0}	1.600×10^{1}
Cu	Cu	4.466×10^{-1}	6.504×10^{0}	8.000×10^{0}
Cu	Cu	4.770×10^{-2}	1.542×10^{1}	2.000×10^{1}
Cu	Cu	5.660×10^{-2}	0.000×10^{0}	2.000×10^{1}
Cu	Cu	5.830×10^{-2}	1.000×10^{1}	2.000×10^{1}
Cu	Cu	6.900×10^{-3}	0.000×10^{0}	1.200×10^{1}
Cu	Cu	7.460×10^{-2}	1.234×10^{1}	1.600×10^{1}
Cu	Cu	8.020×10^{-2}	1.189×10^{1}	2.000×10^{1}
Cu	Mg	1.000×10^{-2}	0.000×10^{0}	2.000×10^{1}
Cu	Mg	1.073×10^{-1}	0.000×10^{0}	1.600×10^{1}
Cu	Mg	1.117×10^{-1}	1.301×10^{1}	1.600×10^{1}
Cu	Mg	1.166×10^{-1}	7.071×10^{0}	2.000×10^{1}
Cu	Mg	1.350×10^{-1}	9.170×10^{0}	2.000×10^{1}
Cu	Mg	1.560×10^{-2}	0.000×10^{0}	8.000×10^{0}
Cu	Mg	1.689×10^{-1}	1.057×10^{1}	1.600×10^{1}
Cu	Mg	2.102×10^{-1}	0.000×10^{0}	8.000×10^{0}
Cu	Mg	2.109×10^{-1}	7.336×10^{0}	1.600×10^{1}
Cu	Mg	2.500×10^{-3}	0.000×10^{0}	2.000×10^{1}

TABLE III. (*Continued.*)

Element1	Element2	η	r_2	r_c
Cu	Mg	2.982×10^{-1}	6.169×10^{0}	8.000×10^{0}
Cu	Mg	3.900×10^{-3}	0.000×10^{0}	1.600×10^{1}
Cu	Mg	4.466×10^{-1}	6.504×10^{0}	8.000×10^{0}
Cu	Mg	4.770×10^{-2}	1.542×10^{1}	2.000×10^{1}
Cu	Mg	5.830×10^{-2}	1.000×10^{1}	2.000×10^{1}
Cu	Mg	6.900×10^{-3}	0.000×10^{0}	1.200×10^{1}
Cu	Mg	7.460×10^{-2}	1.234×10^{1}	1.600×10^{1}
Cu	Mg	8.020×10^{-2}	1.189×10^{1}	2.000×10^{1}
Cu	Zn	1.000×10^{-2}	0.000×10^{0}	2.000×10^{1}
Cu	Zn	1.117×10^{-1}	1.301×10^{1}	1.600×10^{1}
Cu	Zn	1.166×10^{-1}	7.071×10^{0}	2.000×10^{1}
Cu	Zn	1.350×10^{-1}	9.170×10^{0}	2.000×10^{1}
Cu	Zn	1.560×10^{-2}	0.000×10^{0}	8.000×10^{0}
Cu	Zn	1.600×10^{-1}	0.000×10^{0}	2.000×10^{1}
Cu	Zn	1.689×10^{-1}	1.057×10^{1}	1.600×10^{1}
Cu	Zn	2.102×10^{-1}	0.000×10^{0}	8.000×10^{0}
Cu	Zn	2.109×10^{-1}	7.336×10^{0}	1.600×10^{1}
Cu	Zn	2.500×10^{-3}	0.000×10^{0}	2.000×10^{1}
Cu	Zn	2.982×10^{-1}	6.169×10^{0}	8.000×10^{0}
Cu	Zn	3.900×10^{-3}	0.000×10^{0}	1.600×10^{1}
Cu	Zn	4.466×10^{-1}	6.504×10^{0}	8.000×10^{0}
Cu	Zn	4.770×10^{-2}	1.542×10^{1}	2.000×10^{1}
Cu	Zn	5.830×10^{-2}	1.000×10^{1}	2.000×10^{1}
Cu	Zn	6.900×10^{-3}	0.000×10^{0}	1.200×10^{1}
Cu	Zn	7.460×10^{-2}	1.234×10^{1}	1.600×10^{1}
Cu	Zn	8.020×10^{-2}	1.189×10^{1}	2.000×10^{1}
Mg	Al	1.000×10^{-2}	0.000×10^{0}	2.000×10^{1}
Mg	Al	1.073×10^{-1}	0.000×10^{0}	1.600×10^{1}
Mg	Al	1.117×10^{-1}	1.301×10^{1}	1.600×10^{1}
Mg	Al	1.166×10^{-1}	7.071×10^{0}	2.000×10^{1}
Mg	Al	1.350×10^{-1}	9.170×10^{0}	2.000×10^{1}
Mg	Al	1.560×10^{-2}	0.000×10^{0}	8.000×10^{0}
Mg	Al	1.689×10^{-1}	1.057×10^{1}	1.600×10^{1}
Mg	Al	2.102×10^{-1}	0.000×10^{0}	8.000×10^{0}
Mg	Al	2.109×10^{-1}	7.336×10^{0}	1.600×10^{1}
Mg	Al	2.500×10^{-3}	0.000×10^{0}	2.000×10^{1}
Mg	Al	2.982×10^{-1}	6.169×10^{0}	8.000×10^{0}
Mg	Al	3.580×10^{-2}	0.000×10^{0}	8.000×10^{0}
Mg	Al	3.900×10^{-3}	0.000×10^{0}	1.600×10^{1}
Mg	Al	4.466×10^{-1}	6.504×10^{0}	8.000×10^{0}
Mg	Al	4.770×10^{-2}	1.542×10^{1}	2.000×10^{1}
Mg	Al	5.830×10^{-2}	1.000×10^{1}	2.000×10^{1}
Mg	Al	6.900×10^{-3}	0.000×10^{0}	1.200×10^{1}
Mg	Al	7.460×10^{-2}	1.234×10^{1}	1.600×10^{1}
Mg	Al	8.020×10^{-2}	1.189×10^{1}	2.000×10^{1}
Mg	Cu	1.000×10^{-2}	0.000×10^{0}	2.000×10^{1}
Mg	Cu	1.073×10^{-1}	0.000×10^{0}	1.600×10^{1}
Mg	Cu	1.117×10^{-1}	1.301×10^{1}	1.600×10^{1}
Mg	Cu	1.166×10^{-1}	7.071×10^{0}	2.000×10^{1}
Mg	Cu	1.350×10^{-1}	9.170×10^{0}	2.000×10^{1}
Mg	Cu	1.560×10^{-2}	0.000×10^{0}	8.000×10^{0}
Mg	Cu	1.590×10^{-2}	0.000×10^{0}	1.200×10^{1}
Mg	Cu	1.689×10^{-1}	1.057×10^{1}	1.600×10^{1}
Mg	Cu	2.102×10^{-1}	0.000×10^{0}	8.000×10^{0}

TABLE III. (*Continued.*)

Element1	Element2	η	r_2	r_c
Mg	Cu	2.109×10^{-1}	7.336×10^{0}	1.600×10^{1}
Mg	Cu	2.500×10^{-3}	0.000×10^{0}	2.000×10^{1}
Mg	Cu	2.982×10^{-1}	6.169×10^{0}	8.000×10^{0}
Mg	Cu	3.580×10^{-2}	0.000×10^{0}	8.000×10^{0}
Mg	Cu	3.900×10^{-3}	0.000×10^{0}	1.600×10^{1}
Mg	Cu	4.466×10^{-1}	6.504×10^{0}	8.000×10^{0}
Mg	Cu	4.770×10^{-2}	1.542×10^{1}	2.000×10^{1}
Mg	Cu	5.830×10^{-2}	1.000×10^{1}	2.000×10^{1}
Mg	Cu	6.900×10^{-3}	0.000×10^{0}	1.200×10^{1}
Mg	Cu	7.460×10^{-2}	1.234×10^{1}	1.600×10^{1}
Mg	Cu	8.020×10^{-2}	1.189×10^{1}	2.000×10^{1}
Mg	Mg	1.000×10^{-2}	0.000×10^{0}	2.000×10^{1}
Mg	Mg	1.073×10^{-1}	0.000×10^{0}	1.600×10^{1}
Mg	Mg	1.117×10^{-1}	1.301×10^{1}	1.600×10^{1}
Mg	Mg	1.166×10^{-1}	7.071×10^{0}	2.000×10^{1}
Mg	Mg	1.350×10^{-1}	9.170×10^{0}	2.000×10^{1}
Mg	Mg	1.560×10^{-2}	0.000×10^{0}	8.000×10^{0}
Mg	Mg	1.590×10^{-2}	0.000×10^{0}	1.200×10^{1}
Mg	Mg	1.689×10^{-1}	1.057×10^{1}	1.600×10^{1}
Mg	Mg	1.875×10^{-1}	0.000×10^{0}	8.000×10^{0}
Mg	Mg	2.109×10^{-1}	7.336×10^{0}	1.600×10^{1}
Mg	Mg	2.500×10^{-3}	0.000×10^{0}	2.000×10^{1}
Mg	Mg	2.982×10^{-1}	6.169×10^{0}	8.000×10^{0}
Mg	Mg	3.580×10^{-2}	0.000×10^{0}	8.000×10^{0}
Mg	Mg	3.900×10^{-3}	0.000×10^{0}	1.600×10^{1}
Mg	Mg	4.466×10^{-1}	6.504×10^{0}	8.000×10^{0}
Mg	Mg	4.770×10^{-2}	1.542×10^{1}	2.000×10^{1}
Mg	Mg	5.830×10^{-2}	1.000×10^{1}	2.000×10^{1}
Mg	Mg	6.900×10^{-3}	0.000×10^{0}	1.200×10^{1}
Mg	Mg	7.460×10^{-2}	1.234×10^{1}	1.600×10^{1}
Mg	Mg	8.020×10^{-2}	1.189×10^{1}	2.000×10^{1}
Mg	Zn	1.000×10^{-2}	0.000×10^{0}	2.000×10^{1}
Mg	Zn	1.117×10^{-1}	1.301×10^{1}	1.600×10^{1}
Mg	Zn	1.166×10^{-1}	7.071×10^{0}	2.000×10^{1}
Mg	Zn	1.350×10^{-1}	9.170×10^{0}	2.000×10^{1}
Mg	Zn	1.560×10^{-2}	0.000×10^{0}	8.000×10^{0}
Mg	Zn	1.590×10^{-2}	0.000×10^{0}	1.200×10^{1}
Mg	Zn	1.600×10^{-1}	0.000×10^{0}	2.000×10^{1}
Mg	Zn	1.689×10^{-1}	1.057×10^{1}	1.600×10^{1}
Mg	Zn	2.102×10^{-1}	0.000×10^{0}	8.000×10^{0}
Mg	Zn	2.109×10^{-1}	7.336×10^{0}	1.600×10^{1}
Mg	Zn	2.500×10^{-3}	0.000×10^{0}	2.000×10^{1}
Mg	Zn	2.982×10^{-1}	6.169×10^{0}	8.000×10^{0}
Mg	Zn	3.900×10^{-3}	0.000×10^{0}	1.600×10^{1}
Mg	Zn	4.466×10^{-1}	6.504×10^{0}	8.000×10^{0}
Mg	Zn	4.770×10^{-2}	1.542×10^{1}	2.000×10^{1}
Mg	Zn	5.830×10^{-2}	1.000×10^{1}	2.000×10^{1}
Mg	Zn	6.900×10^{-3}	0.000×10^{0}	1.200×10^{1}
Mg	Zn	7.460×10^{-2}	1.234×10^{1}	1.600×10^{1}
Mg	Zn	8.020×10^{-2}	1.189×10^{1}	2.000×10^{1}
Zn	Al	1.000×10^{-2}	0.000×10^{0}	2.000×10^{1}
Zn	Al	1.117×10^{-1}	1.301×10^{1}	1.600×10^{1}
Zn	Al	1.166×10^{-1}	7.071×10^{0}	2.000×10^{1}
Zn	Al	1.350×10^{-1}	9.170×10^{0}	2.000×10^{1}

TABLE III. (*Continued.*)

Element1	Element2	η	r_2	r_c
Zn	Al	1.560×10^{-2}	0.000×10^{0}	8.000×10^{0}
Zn	Al	1.600×10^{-1}	0.000×10^{0}	2.000×10^{1}
Zn	Al	1.689×10^{-1}	1.057×10^{1}	1.600×10^{1}
Zn	Al	2.102×10^{-1}	0.000×10^{0}	8.000×10^{0}
Zn	Al	2.109×10^{-1}	7.336×10^{0}	1.600×10^{1}
Zn	Al	2.500×10^{-3}	0.000×10^{0}	2.000×10^{1}
Zn	Al	2.982×10^{-1}	6.169×10^{0}	8.000×10^{0}
Zn	Al	3.580×10^{-2}	0.000×10^{0}	8.000×10^{0}
Zn	Al	3.900×10^{-3}	0.000×10^{0}	1.600×10^{1}
Zn	Al	4.466×10^{-1}	6.504×10^{0}	8.000×10^{0}
Zn	Al	4.770×10^{-2}	1.542×10^{1}	2.000×10^{1}
Zn	Al	5.830×10^{-2}	1.000×10^{1}	2.000×10^{1}
Zn	Al	6.900×10^{-3}	0.000×10^{0}	1.200×10^{1}
Zn	Al	7.460×10^{-2}	1.234×10^{1}	1.600×10^{1}
Zn	Al	8.020×10^{-2}	1.189×10^{1}	2.000×10^{1}
Zn	Cu	1.000×10^{-2}	0.000×10^{0}	2.000×10^{1}
Zn	Cu	1.117×10^{-1}	1.301×10^{1}	1.600×10^{1}
Zn	Cu	1.166×10^{-1}	7.071×10^{0}	2.000×10^{1}
Zn	Cu	1.350×10^{-1}	9.170×10^{0}	2.000×10^{1}
Zn	Cu	1.560×10^{-2}	0.000×10^{0}	8.000×10^{0}
Zn	Cu	1.600×10^{-1}	0.000×10^{0}	2.000×10^{1}
Zn	Cu	1.689×10^{-1}	1.057×10^{1}	1.600×10^{1}
Zn	Cu	2.102×10^{-1}	0.000×10^{0}	8.000×10^{0}
Zn	Cu	2.109×10^{-1}	7.336×10^{0}	1.600×10^{1}
Zn	Cu	2.500×10^{-3}	0.000×10^{0}	2.000×10^{1}
Zn	Cu	2.982×10^{-1}	6.169×10^{0}	8.000×10^{0}
Zn	Cu	3.536×10^{-1}	0.000×10^{0}	8.000×10^{0}
Zn	Cu	3.580×10^{-2}	0.000×10^{0}	8.000×10^{0}
Zn	Cu	3.900×10^{-3}	0.000×10^{0}	1.600×10^{1}
Zn	Cu	4.466×10^{-1}	6.504×10^{0}	8.000×10^{0}
Zn	Cu	4.770×10^{-2}	1.542×10^{1}	2.000×10^{1}
Zn	Cu	5.830×10^{-2}	1.000×10^{1}	2.000×10^{1}
Zn	Cu	6.900×10^{-3}	0.000×10^{0}	1.200×10^{1}
Zn	Cu	7.460×10^{-2}	1.234×10^{1}	1.600×10^{1}
Zn	Cu	8.020×10^{-2}	1.189×10^{1}	2.000×10^{1}
Zn	Mg	1.000×10^{-2}	0.000×10^{0}	2.000×10^{1}
Zn	Mg	1.117×10^{-1}	1.301×10^{1}	1.600×10^{1}
Zn	Mg	1.166×10^{-1}	7.071×10^{0}	2.000×10^{1}
Zn	Mg	1.350×10^{-1}	9.170×10^{0}	2.000×10^{1}
Zn	Mg	1.560×10^{-2}	0.000×10^{0}	8.000×10^{0}
Zn	Mg	1.600×10^{-1}	0.000×10^{0}	2.000×10^{1}
Zn	Mg	1.689×10^{-1}	1.057×10^{1}	1.600×10^{1}
Zn	Mg	2.102×10^{-1}	0.000×10^{0}	8.000×10^{0}
Zn	Mg	2.109×10^{-1}	7.336×10^{0}	1.600×10^{1}
Zn	Mg	2.500×10^{-3}	0.000×10^{0}	2.000×10^{1}
Zn	Mg	2.982×10^{-1}	6.169×10^{0}	8.000×10^{0}
Zn	Mg	3.580×10^{-2}	0.000×10^{0}	8.000×10^{0}
Zn	Mg	3.900×10^{-3}	0.000×10^{0}	1.600×10^{1}
Zn	Mg	4.466×10^{-1}	6.504×10^{0}	8.000×10^{0}
Zn	Mg	4.770×10^{-2}	1.542×10^{1}	2.000×10^{1}
Zn	Mg	5.830×10^{-2}	1.000×10^{1}	2.000×10^{1}
Zn	Mg	6.900×10^{-3}	0.000×10^{0}	1.200×10^{1}
Zn	Mg	7.460×10^{-2}	1.234×10^{1}	1.600×10^{1}

TABLE III. (*Continued.*)

Element1	Element2	η	r_2	r_c
Zn	Mg	8.020×10^{-2}	1.189×10^{1}	2.000×10^{1}
Zn	Zn	1.000×10^{-2}	0.000×10^{0}	2.000×10^{1}
Zn	Zn	1.117×10^{-1}	1.301×10^{1}	1.600×10^{1}
Zn	Zn	1.166×10^{-1}	7.071×10^{0}	2.000×10^{1}
Zn	Zn	1.254×10^{-1}	9.514×10^{0}	1.600×10^{1}
Zn	Zn	1.350×10^{-1}	9.170×10^{0}	2.000×10^{1}
Zn	Zn	1.560×10^{-2}	0.000×10^{0}	8.000×10^{0}
Zn	Zn	1.590×10^{-2}	0.000×10^{0}	1.200×10^{1}
Zn	Zn	1.600×10^{-1}	0.000×10^{0}	2.000×10^{1}
Zn	Zn	1.689×10^{-1}	1.057×10^{1}	1.600×10^{1}
Zn	Zn	2.109×10^{-1}	7.336×10^{0}	1.600×10^{1}
Zn	Zn	2.500×10^{-3}	0.000×10^{0}	2.000×10^{1}
Zn	Zn	2.837×10^{-1}	0.000×10^{0}	8.000×10^{0}
Zn	Zn	2.910×10^{-2}	1.414×10^{1}	2.000×10^{1}
Zn	Zn	2.982×10^{-1}	6.169×10^{0}	8.000×10^{0}
Zn	Zn	3.580×10^{-2}	0.000×10^{0}	8.000×10^{0}
Zn	Zn	3.900×10^{-3}	0.000×10^{0}	1.600×10^{1}
Zn	Zn	4.466×10^{-1}	6.504×10^{0}	8.000×10^{0}
Zn	Zn	4.770×10^{-2}	1.542×10^{1}	2.000×10^{1}
Zn	Zn	5.830×10^{-2}	1.000×10^{1}	2.000×10^{1}
Zn	Zn	6.900×10^{-3}	0.000×10^{0}	1.200×10^{1}
Zn	Zn	7.460×10^{-2}	1.234×10^{1}	1.600×10^{1}
Zn	Zn	8.020×10^{-2}	1.189×10^{1}	2.000×10^{1}
Zn	Zn	9.510×10^{-2}	0.000×10^{0}	2.000×10^{1}

TABLE IV. Hyperparameters for the angular symmetry functions added by CURSEL for Al-Cu-Mg-Zn NNPs.

Element1	Element2	Element3	η	λ	ζ	r_c
Al	Al	Al	1.350×10^{-2}	1	1.0	1.600×10^{1}
Al	Al	Al	3.900×10^{-3}	–1	1.0	1.600×10^{1}
Al	Al	Al	3.900×10^{-3}	1	1.0	1.600×10^{1}
Al	Al	Al	3.900×10^{-3}	1	4.0	1.600×10^{1}
Al	Al	Cu	1.350×10^{-2}	1	1.0	1.600×10^{1}
Al	Al	Cu	3.900×10^{-3}	–1	1.0	1.600×10^{1}
Al	Al	Cu	3.900×10^{-3}	1	1.0	1.600×10^{1}
Al	Al	Cu	3.900×10^{-3}	1	4.0	1.600×10^{1}
Al	Al	Zn	3.900×10^{-3}	–1	1.0	1.600×10^{1}
Al	Al	Zn	3.900×10^{-3}	1	1.0	1.600×10^{1}
Al	Cu	Cu	3.900×10^{-3}	1	1.0	1.600×10^{1}
Al	Cu	Zn	3.900×10^{-3}	1	1.0	1.600×10^{1}
Al	Mg	Al	3.900×10^{-3}	–1	1.0	1.600×10^{1}
Al	Mg	Al	3.900×10^{-3}	1	1.0	1.600×10^{1}
Al	Mg	Cu	3.900×10^{-3}	1	1.0	1.600×10^{1}
Al	Mg	Mg	3.900×10^{-3}	1	1.0	1.600×10^{1}
Al	Mg	Zn	3.900×10^{-3}	1	1.0	1.600×10^{1}
Al	Zn	Zn	3.900×10^{-3}	1	1.0	1.600×10^{1}
Cu	Al	Al	3.900×10^{-3}	1	1.0	1.600×10^{1}

TABLE IV. (*Continued.*)

Element1	Element2	Element3	η	λ	ζ	r_c
Cu	Al	Cu	1.350×10^{-2}	1	1.0	1.600×10^{1}
Cu	Al	Cu	3.900×10^{-3}	–1	1.0	1.600×10^{1}
Cu	Al	Cu	3.900×10^{-3}	1	1.0	1.600×10^{1}
Cu	Al	Cu	3.900×10^{-3}	1	4.0	1.600×10^{1}
Cu	Al	Zn	3.900×10^{-3}	–1	1.0	1.600×10^{1}
Cu	Al	Zn	3.900×10^{-3}	1	1.0	1.600×10^{1}
Cu	Cu	Cu	1.350×10^{-2}	1	1.0	1.600×10^{1}
Cu	Cu	Cu	3.900×10^{-3}	–1	1.0	1.600×10^{1}
Cu	Cu	Cu	3.900×10^{-3}	1	1.0	1.600×10^{1}
Cu	Cu	Zn	3.900×10^{-3}	–1	1.0	1.600×10^{1}
Cu	Cu	Zn	3.900×10^{-3}	1	1.0	1.600×10^{1}
Cu	Mg	Al	1.350×10^{-2}	1	1.0	1.600×10^{1}
Cu	Mg	Al	3.900×10^{-3}	–1	1.0	1.600×10^{1}
Cu	Mg	Al	3.900×10^{-3}	1	1.0	1.600×10^{1}
Cu	Mg	Cu	3.900×10^{-3}	–1	1.0	1.600×10^{1}
Cu	Mg	Cu	3.900×10^{-3}	1	1.0	1.600×10^{1}
Cu	Mg	Mg	3.900×10^{-3}	1	1.0	1.600×10^{1}
Cu	Mg	Zn	3.900×10^{-3}	1	1.0	1.600×10^{1}
Cu	Zn	Zn	3.900×10^{-3}	–1	1.0	1.600×10^{1}
Cu	Zn	Zn	3.900×10^{-3}	1	1.0	1.600×10^{1}
Mg	Al	Al	3.900×10^{-3}	1	1.0	1.600×10^{1}
Mg	Al	Cu	3.900×10^{-3}	–1	1.0	1.600×10^{1}
Mg	Al	Cu	3.900×10^{-3}	1	1.0	1.600×10^{1}
Mg	Al	Zn	3.900×10^{-3}	1	1.0	1.600×10^{1}
Mg	Cu	Cu	3.900×10^{-3}	1	1.0	1.600×10^{1}
Mg	Cu	Zn	3.900×10^{-3}	–1	1.0	1.600×10^{1}
Mg	Cu	Zn	3.900×10^{-3}	1	1.0	1.600×10^{1}
Mg	Mg	Al	1.350×10^{-2}	1	1.0	1.600×10^{1}
Mg	Mg	Al	3.900×10^{-3}	–1	1.0	1.600×10^{1}
Mg	Mg	Al	3.900×10^{-3}	1	1.0	1.600×10^{1}
Mg	Mg	Cu	1.350×10^{-2}	1	1.0	1.600×10^{1}
Mg	Mg	Cu	3.900×10^{-3}	–1	1.0	1.600×10^{1}
Mg	Mg	Cu	3.900×10^{-3}	1	1.0	1.600×10^{1}
Mg	Mg	Mg	3.900×10^{-3}	1	1.0	1.600×10^{1}
Mg	Mg	Zn	3.900×10^{-3}	–1	1.0	1.600×10^{1}
Mg	Mg	Zn	3.900×10^{-3}	1	1.0	1.600×10^{1}
Mg	Zn	Zn	3.900×10^{-3}	–1	1.0	1.600×10^{1}
Mg	Zn	Zn	3.900×10^{-3}	1	1.0	1.600×10^{1}
Zn	Al	Al	3.900×10^{-3}	1	1.0	1.600×10^{1}
Zn	Al	Cu	3.900×10^{-3}	–1	1.0	1.600×10^{1}
Zn	Al	Cu	3.900×10^{-3}	1	1.0	1.600×10^{1}
Zn	Al	Zn	3.900×10^{-3}	–1	1.0	1.600×10^{1}
Zn	Al	Zn	3.900×10^{-3}	1	1.0	1.600×10^{1}
Zn	Cu	Cu	3.900×10^{-3}	1	1.0	1.600×10^{1}
Zn	Cu	Zn	3.900×10^{-3}	–1	1.0	1.600×10^{1}
Zn	Cu	Zn	3.900×10^{-3}	1	1.0	1.600×10^{1}
Zn	Mg	Al	3.900×10^{-3}	1	1.0	1.600×10^{1}
Zn	Mg	Cu	3.900×10^{-3}	1	1.0	1.600×10^{1}
Zn	Mg	Mg	3.900×10^{-3}	1	1.0	1.600×10^{1}
Zn	Mg	Zn	3.900×10^{-3}	1	1.0	1.600×10^{1}
Zn	Zn	Zn	1.350×10^{-2}	1	1.0	1.600×10^{1}
Zn	Zn	Zn	3.900×10^{-3}	–1	1.0	1.600×10^{1}
Zn	Zn	Zn	3.900×10^{-3}	1	1.0	1.600×10^{1}

TABLE V. Hyperparameters for the angular symmetry functions manually added from previous work for both Al-Cu-Mg and Al-Cu-Mg-Zn NNPs.

Element1	Element2	Element3	η	λ	ζ	r_c
Al	Al	Al	7.000×10^{-3}	1	1.0	1.200×10^{2}
Al	Al	Al	7.000×10^{-3}	–1	1.0	1.200×10^{2}
Al	Al	Al	1.600×10^{-2}	1	1.0	8.000×10^{2}
Al	Al	Al	7.000×10^{-3}	1	4.0	1.200×10^{2}
Al	Al	Al	1.600×10^{-2}	–1	1.0	8.000×10^{1}

APPENDIX B: t-SNE ANALYSIS OF AlCuMg DATASET

In Fig. 19 we show a mapping of all the structures via the t-SNE [81] method. The t-SNE method is an embedding method wherein it attempts to preserve the distances between points in high-dimensional space, in our case a 197-dimensional space of all SFs, into a lower dimensional space, wherein the distances between nearby objects in the high-dimensional space are preserved in the lower dimensional embedding. This method does not, however, preserve long-range distances therefore clusters only indicate groups of structures that are similar to each other but clusters that are far apart from each other may not mean the structures are substantially different.

In Fig. 19(a) we see all the structures colored by their order in the original 11 620 structure database and labeled by structure group. We see that t-SNE is able to broadly categorize the different groups, e.g., we see that the randomized Al-Cu, Mg-Cu, and Al-Cu-Mg supercell structures form broad local clusters varying by composition. In Fig. 19(b) we see the structures that were selected to be kept or removed by the FPS method. We see that most of the structures selected for removal are from the "OQMD Bulk" category, this is expected

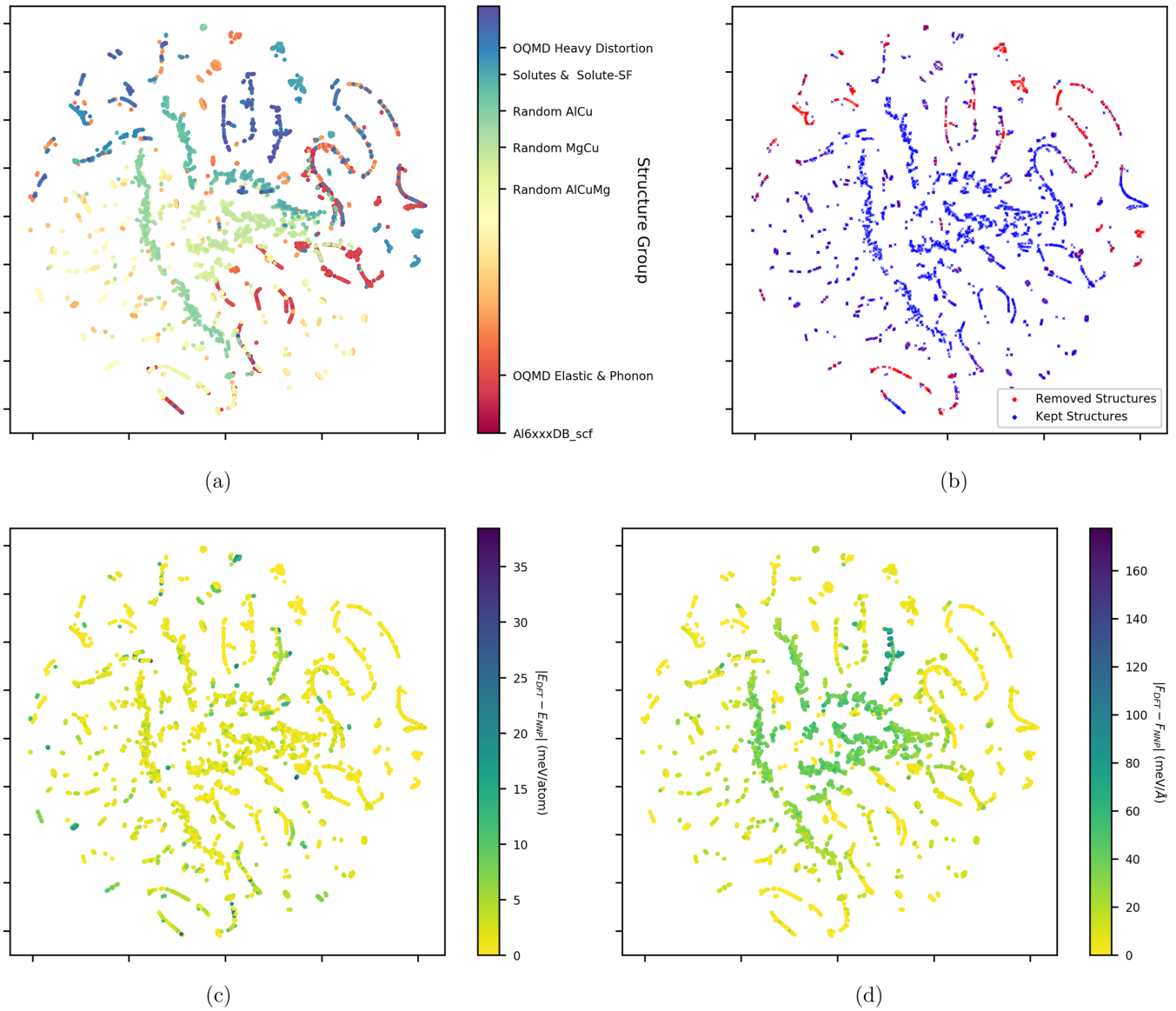

FIG. 19. Structures mapped in two dimensions using the t-SNE method (perplexity = 30) with structures colored by (a) their index within the database, with key categories labeled (b) whether the structure is included or rejected by the FPS method (c) the error in energy for the structure (d) the average force error for the structure.

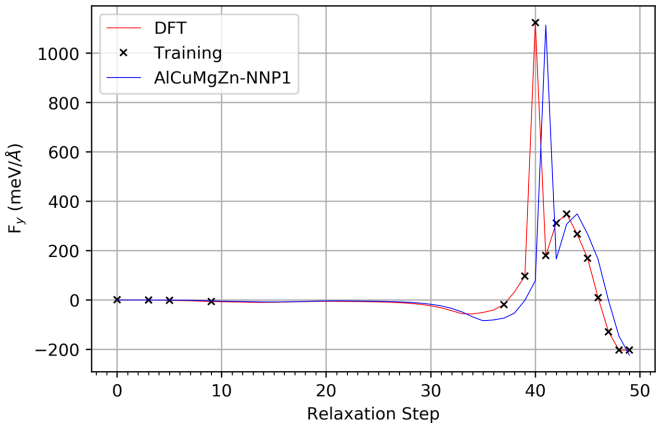

FIG. 20. Force in the y direction vs relaxation step for DFT and AlCuMgZn-NNP1 on atom 8 for η_I' Mg4(Zn5Cu)(Al7Zn) as it relaxes into η_{IV}' form. Only the points marked with x are eligible for training and of these only 2.1% are used in a given epoch. The NNP results are computed using structures taken from the DFT relaxation.

because many of these structures are very similar to each other differing only by small elastic distortions or by small atomic displacements for the phonon dataset. We see that FPS largely keeps all the randomized supercells as these structures are more likely to be sufficiently different or diverse from each other so that each carries relatively unique structural information. FPS also keeps most of the Al-Mg-Si structures from the dataset by Kobayashi *et. al* [5], this too makes sense because these structures have been pre-screened via a FPS selection process prior to inclusion in this database. In Figs. 19(c)–19(d) we see these same structures but colored by their energy and force errors. Energetic errors are largely randomly distributed while force errors tend to be higher in the fully randomized supercell calculations.

APPENDIX C: DFT VS NNP FOR FORCE ERROR DURING RELAXATION

In Fig. 20 we see an example of a situation where the NNP can have very high ($\approx$1 eV/Å) errors in the forces while still respecting the overall dynamics of the system. We focus on the y component of forces on atom 8 because this is where some of the greatest force errors for the entire system occur. We see that there is a massive spike in the y direction of forces in DFT at timestep 40, which does not have a correspondingly high force using the NNP and in the the next relaxation. While the errors at timesteps 40 and 41 are massive, we see that the NNP still respects the overall shape, and even predicts roughly same maximum force. Note that we do not export all structures during relaxation for training, since many have little difference, see steps 10–30 especially, when we dump structures we only use those that have at least 0.5 eV difference in energy for the entire structure. Importantly if we take the same starting structure and relax with AlCuMgZn-NNP1 we see that the structure still undergoes the same transformation as it would under DFT.

APPENDIX D: ERROR HISTORGRAM FOR ALCUMGZN-NNP1 BEFORE AND AFTER SECONDARY TRAINING

In Fig. 21 of this section we show the distribution of errors after secondary training.

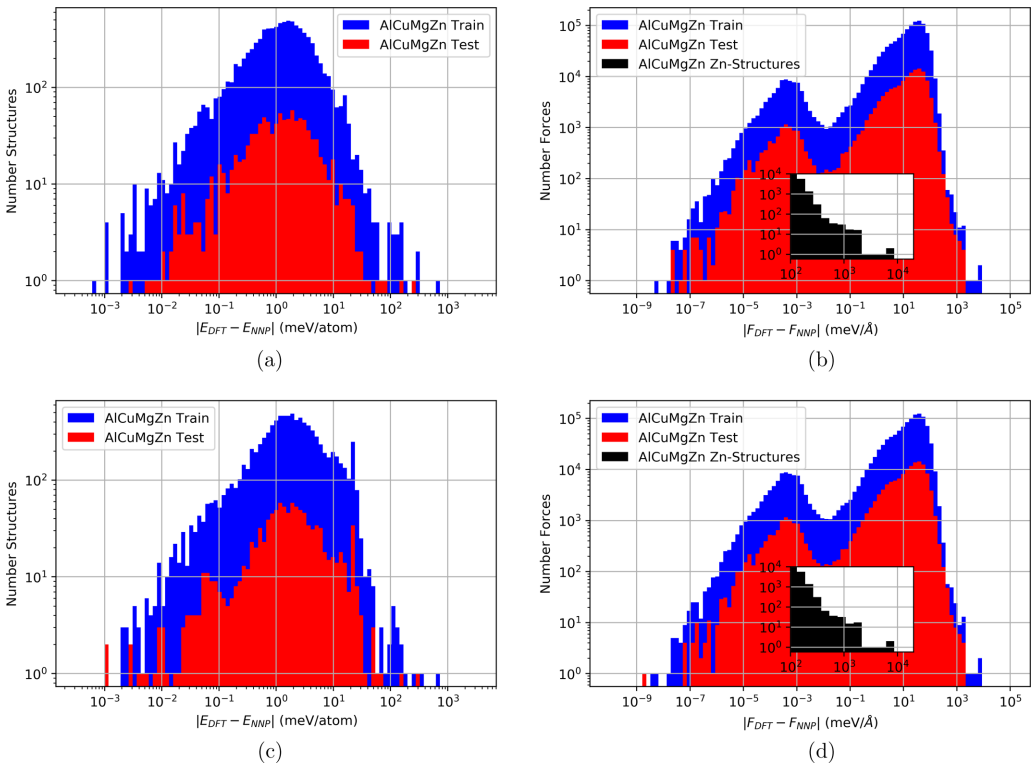

FIG. 21. Histogram of errors for the energies and forces both before [(a),(b)] and after [(c),(d)] secondary training on a the focused dataset for AlZnCuMg NNP1.

APPENDIX E: COMPARISON OF DILUTE SOLUTE ENERGIES TO DFT BEFORE AND AFTER SECONDARY TRAINING

In Fig. 22 of this section we show how secondary training improves the peformance of dilute Zn solute energies for the NNPs.

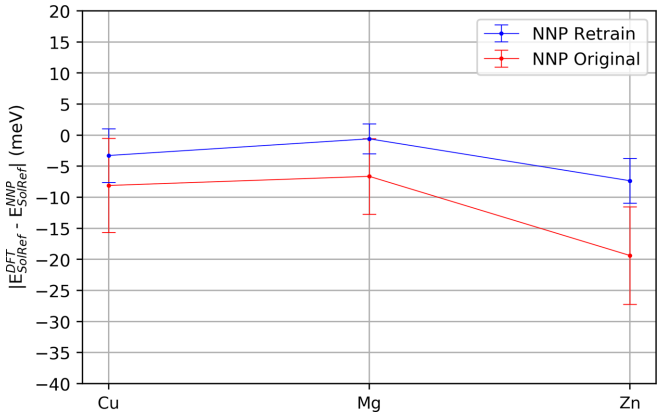

FIG. 22. Comparison of energies for of a single-atom of Cu, Mg, and Zn solute in 256 Al atom supercell to DFT.

APPENDIX F: NNP BENCHMARKS ON Zn-CONTAINING OQMD STRUCTURES

Here, in Fig. 23–28, we show benchmarks for all Zn-containing compounds taken from the OQMD that are not shown in the main text.

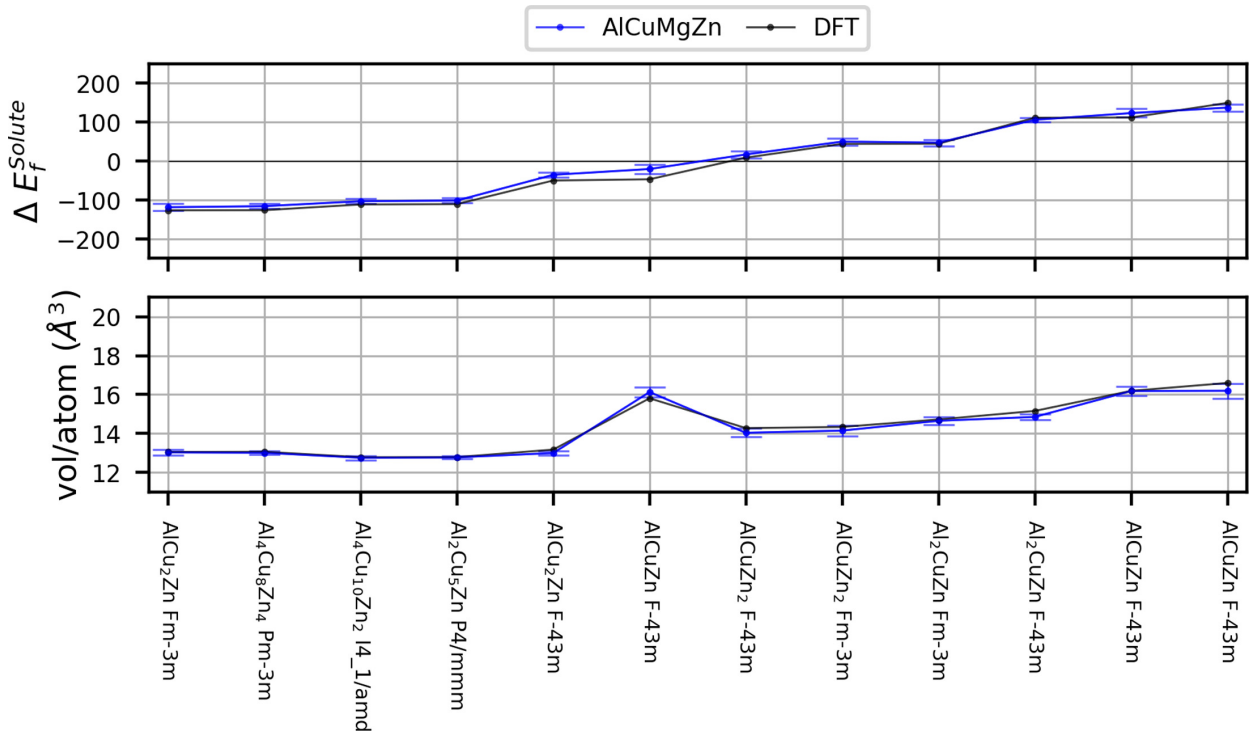

FIG. 23. Formation energy and atomic volume as predicted by DFT, and the NNPs versus structure, for all Al-Cu-Zn structures in the OQMD database. All structures from which these properties are derived are included in the training set.

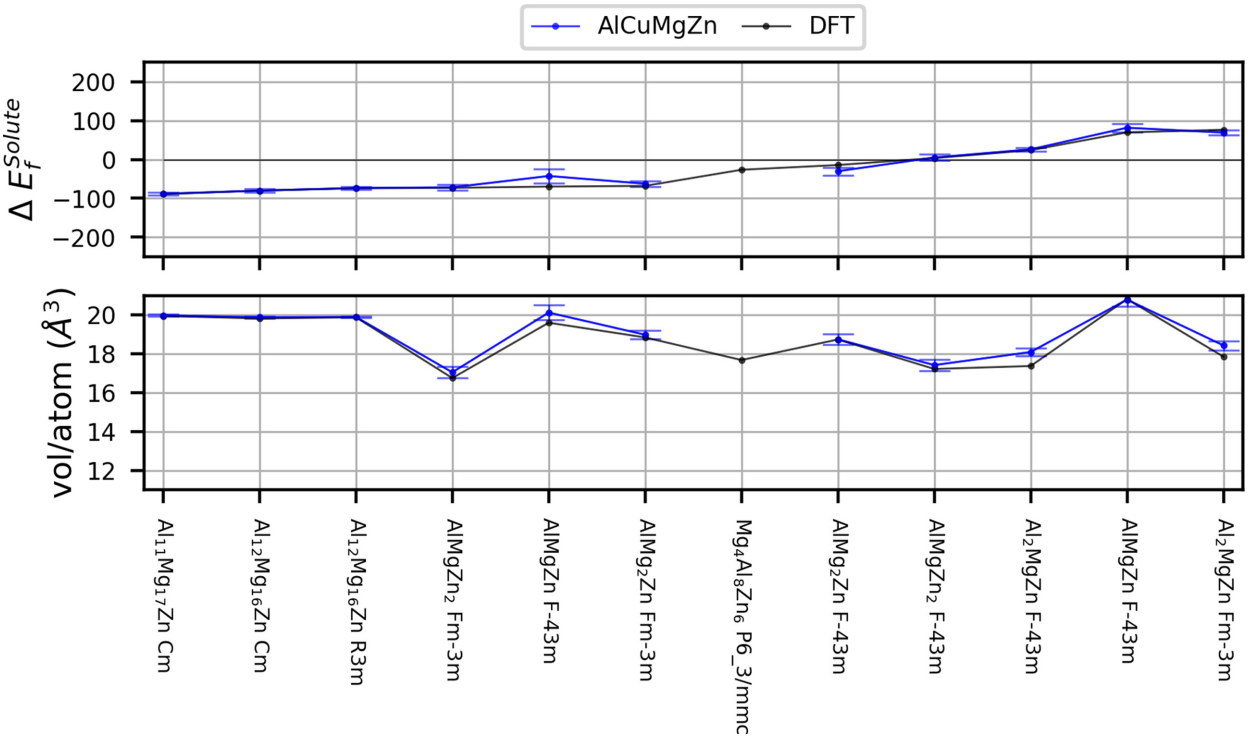

FIG. 24. Formation energy and atomic volume as predicted by DFT, and the NNPs versus structure, for all Al-Mg-Zn structures in the OQMD database. All structures from which these properties are derived are included in the training set.

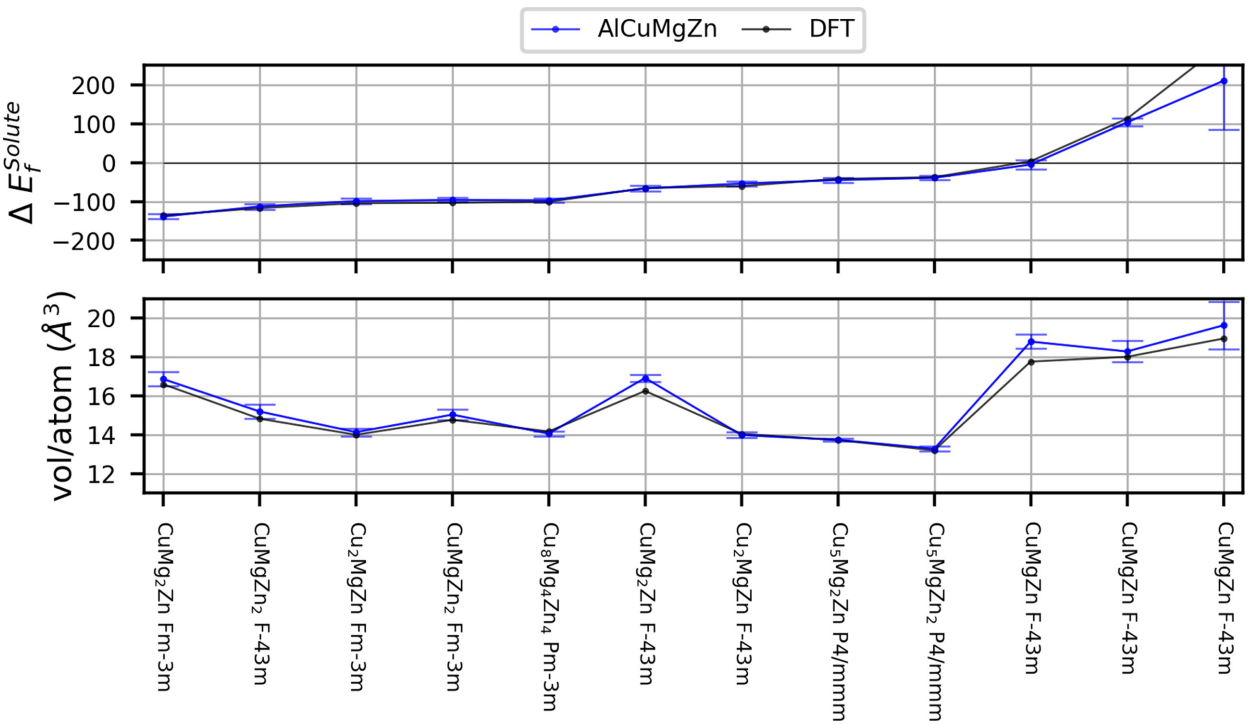

FIG. 25. Formation energy and atomic volume as predicted by DFT, and the NNPs versus structure, for all Cu-Mg-Zn structures in the OQMD database. All structures from which these properties are derived are included in the training set.

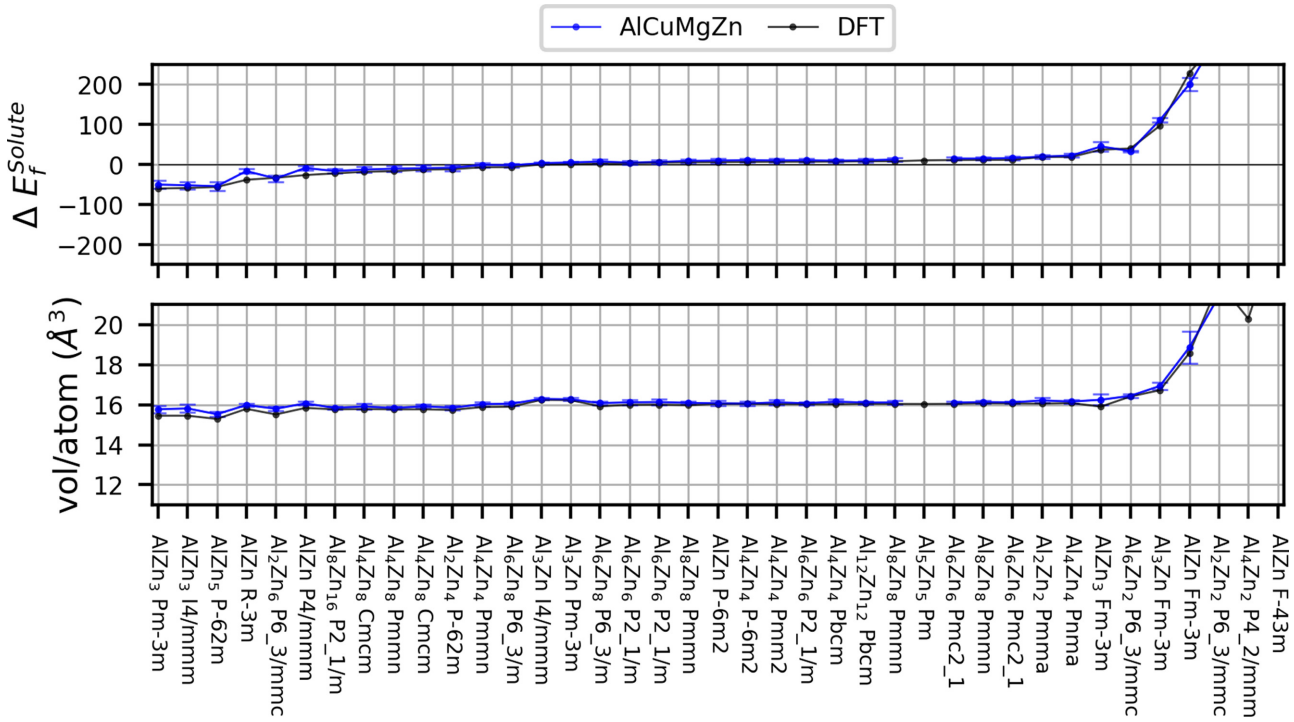

FIG. 26. Formation energy and atomic volume as predicted by DFT, and the NNPs versus structure, for all Al-Zn structures in the OQMD database. All structures from which these properties are derived are included in the training set.

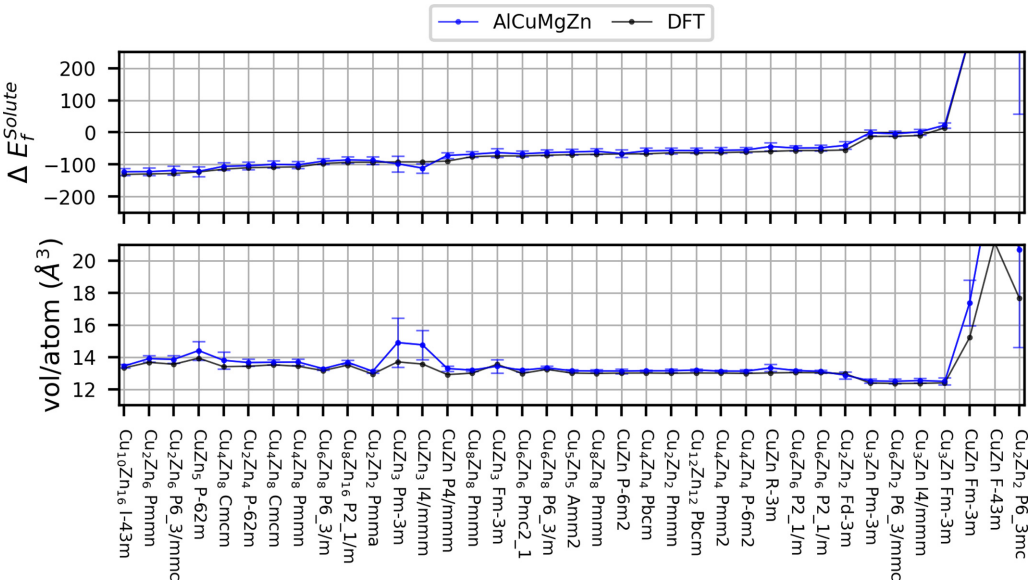

FIG. 27. Formation energy and atomic volume as predicted by DFT, and the NNPs versus structure, for all Cu-Zn structures in the OQMD database. All structures from which these properties are derived are included in the training set.

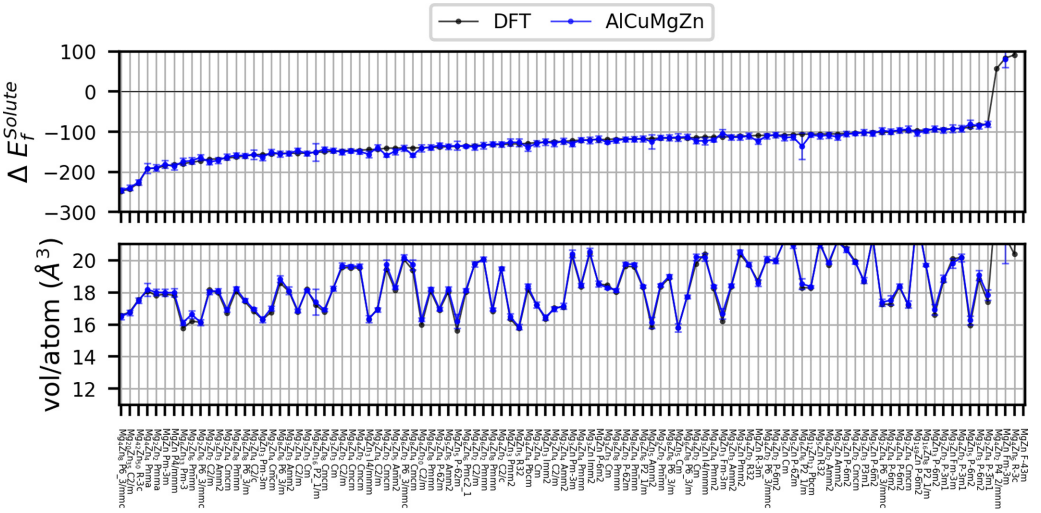

FIG. 28. Formation energy and atomic volume as predicted by DFT, and the NNPs versus structure, for all Mg-Zn structures in the OQMD database. All structures from which these properties are derived are included in the training set.

APPENDIX G: SPHASE INTERFACE

In Fig. 29 of this section we show both a schematic of the Sphase interface, along with energy validation for the NNPs.

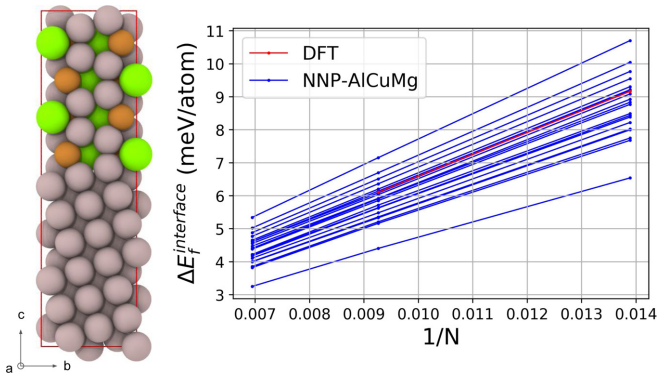

FIG. 29. Image of S/Al interface (left) where a = 4.03 Å, b = 9.17 Å, and c varies with the number of S and Al units (in this figure c = 32.26 Å). Grey atoms are Al, brown atoms are Cu and green atoms are Mg. Plot of $\Delta E_{\text{interface}}$ vs $1/N$ showing good agreement between DFT and NNPs on the slope.

APPENDIX H: GSF FOR θ'' and θ

Here, in Figs. 30 and 31, we show the GSF energy benchmarks for the NNPs for both the θ'' and θ phases.

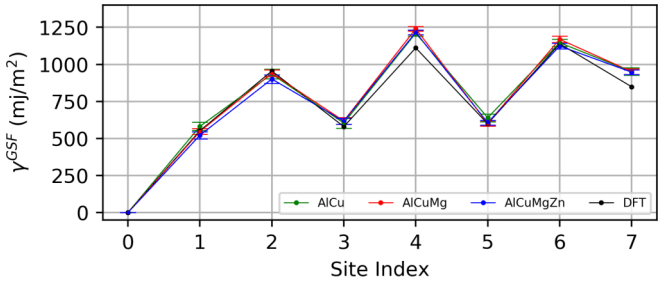

FIG. 30. Validation of key points on the θ GSF surface for DFT and NNPs. These structures are not included in the training set.

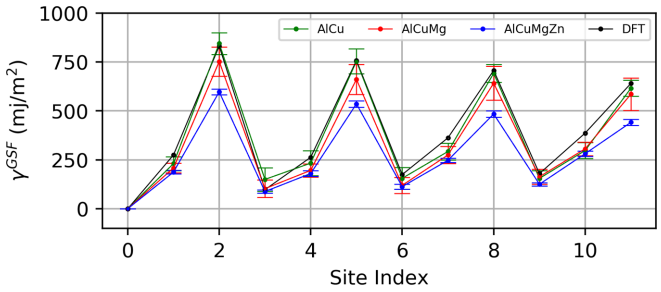

FIG. 31. Validation of key points on the θ'' GSF surface for DFT and NNPs. These structures are not included in the training set.

APPENDIX I: LJ TERM FOR INTERATOMIC POTENTIAL

As discussed in the main text, the major errors in the NNP are found for very close atomic distances. In this short-range domain, the NNP energies can become strongly negative, driving the system to collapse toward zero atomic spacings. Since the potentials are repulsive at larger distances, such short distances would rarely, if ever, be present in most applications governed by thermodynamics. However, when atoms are placed in positions a priori, such as in defining an initial path for a transition state analysis or an initial configuration for computing a fault energy, atoms can be placed close together and the serious failure of the NNP can lead to problems for these types of applications. To avoid pathological results, in principle, more structures with close atom spacings could be added to the set of training structures. Because these structures would have high energy, they could adversely affect the quality of the the NNP in the domains of physical interest. Another solution, demonstrated here, is to simply add an ad-hoc repulsive cut-and-shifted Lennard-Jones (LJ) potential at short distances to counteract the deficiencies of the NNP.

Specifically, we introduce a cut-and-shifted LJ potential to create a purely repulsive potential. The potential between atoms i ad j at distance r is taken to be

$$LJ_{i,j}(r) = \begin{cases} 4\epsilon\left[\left(\frac{\sigma_{i,j}}{r}\right)^{12} - \left(\frac{\sigma_{i,j}}{r}\right)^{6}\right] + 4\epsilon, & r \leqslant r_{\text{cut}} \\ 0, & r > r_{\text{cut}} \end{cases} \tag{I1}$$

where $r_{\text{cut}} = 2^{\frac{1}{6}}\sigma$. For a ternary alloy, we have 6 LJ functions, and we use a common energy scale $\epsilon = 20(eV)$ and pair-specific distances $\sigma_{i,j}$. We choose $r_{\text{cut}} = 0.85 r_{0,ij}$ where $r_{0,ij} j = i$ is the bulk interatomic distance for atom i given in the ASE [43] package. For unlike pairs $j \neq i$, we use $r_{0,ij} = 0.5(r_{0,ii} + r_{0,jj})$.

APPENDIX J: Al-Cu ANTISITE ENERGIES

Here, in Fig. 32, we confirm the good peformance of AlCuMgZn NNPs for Al-Cu antsite energies.

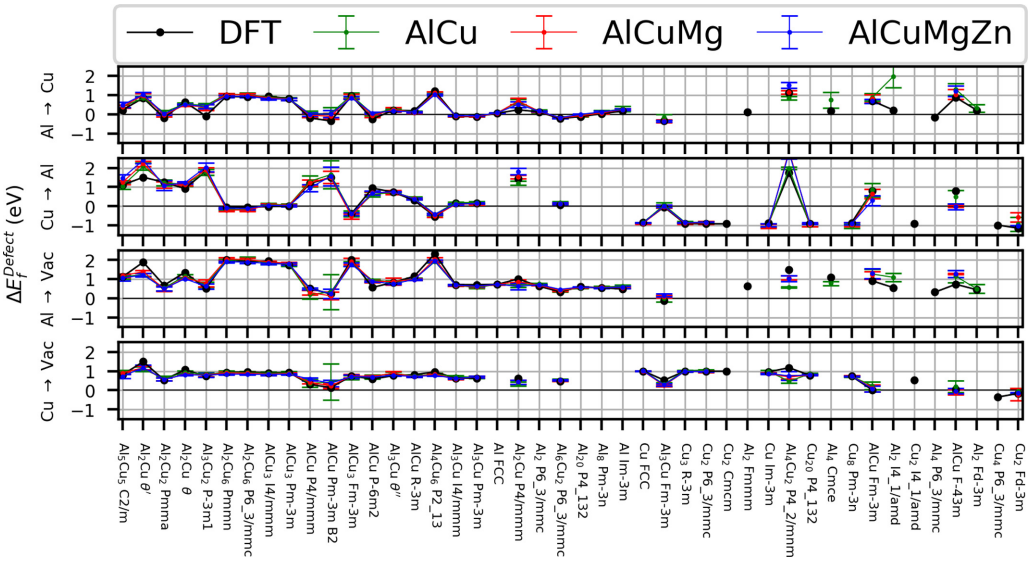

FIG. 32. DFT antisite formation energy vs NNP antisite formation energy for Al-Cu compounds. These structures are not included in the training set.

[1] C. Wolverton and V. Ozoliņš, Phys. Rev. Lett. **86**, 5518 (2001).
[2] D. Marchand, A. Jain, A. Glensk, and W. A. Curtin, Phys. Rev. Materials **4**, 103601 (2020).
[3] M. Stricker, B. Yin, E. Mak, and W. A. Curtin, Phys. Rev. Materials **4**, 103602 (2020).
[4] A. C. P. Jain, D. Marchand, A. Glensk, M. Ceriotti, and W. A. Curtin, Phys. Rev. Materials **5**, 053805 (2021).
[5] R. Kobayashi, D. Giofré, T. Junge, M. Ceriotti, and W. A. Curtin, Phys. Rev. Materials **1**, 053604 (2017).
[6] M. S. Nitol, D. E. Dickel, and C. D. Barrett, Comput. Mater. Sci. **188**, 110207 (2021).
[7] M. S. Nitol, D. E. Dickel, and C. D. Barrett, Acta Mater. **224**, 117347 (2022).
[8] F. S. Meng, J. P. Du, S. Shinzato, H. Mori, P. Yu, K. Matsubara, N. Ishikawa, and S. Ogata, Phys. Rev. Materials **5**, 113606 (2021).
[9] G. Imbalzano and M. Ceriotti, Phys. Rev. Materials **5**, 063804 (2021).
[10] G. Sivaraman, L. Gallington, A. N. Krishnamoorthy, M. Stan, G. Csanyi, A. Vazquez-Mayagoitia, and C. J. Benmore, Phys. Rev. Lett. **126**, 156002 (2021).
[11] M. Hodapp and A. Shapeev, Phys. Rev. Materials **5**, 113802 (2021).
[12] S. Yin, Y. Zuo, A. Abu-Odeh, H. Zheng, X.-G. Li, J. Ding, S. P. Ong, M. Asta, and R. O. Ritchie, Nat. Commun. **12**, 4873 (2021).
[13] X. G. Li, C. Chen, H. Zheng, Y. Zuo, and S. P. Ong, npj Comput. Mater. **6**, 70 (2020).
[14] Y. Mishin, Acta Mater. **214**, 116980 (2021).
[15] J. Behler, Chem. Rev. **121**, 10037 (2021).
[16] P. Friederich, F. Häse, J. Proppe, and A. Aspuru-Guzik, Nat. Mater. **20**, 750 (2021).
[17] J. Behler and M. Parrinello, Phys. Rev. Lett. **98**, 146401 (2007).
[18] A. P. Bartók, R. Kondor, and G. Csányi, Phys. Rev. B **87**, 184115 (2013).
[19] R. Drautz, Phys. Rev. B **99**, 014104 (2019).
[20] T. Xie and J. C. Grossman, Phys. Rev. Lett. **120**, 145301 (2018).
[21] G. P. Purja Pun, R. Batra, R. Ramprasad, and Y. Mishin, Nat. Commun. **10**, 2339 (2019).
[22] G. P. Purja Pun, V. Yamakov, J. Hickman, E. H. Glaessgen, and Y. Mishin, Phys. Rev. Materials **4**, 113807 (2020).
[23] L. Zhang, D.-Y. Lin, H. Wang, R. Car, and W. E., Phys. Rev. Materials **3**, 023804 (2019).
[24] J. S. Smith, B. Nebgen, N. Mathew, J. Chen, N. Lubbers, L. Burakovsky, S. Tretiak, H. A. Nam, T. Germann, S. Fensin, and K. Barros, Nat. Commun. **12**, 1257 (2020).
[25] T. L. Jacobsen, M. S. Jørgensen, and B. Hammer, Phys. Rev. Lett. **120**, 026102 (2018).
[26] N. Bernstein, G. Csányi, and V. L. Deringer, npj Comput. Mater. **5**, 99 (2019).
[27] V. L. Deringer, C. J. Pickard, and G. Csányi, Phys. Rev. Lett. **120**, 156001 (2018).
[28] J.-F. Nie, *in Physical Metallurgy*, edited by D. E. Laughlin and K. Hono (Elsevier, New York, 2014), pp. 2009–2156.
[29] A. Lervik, E. Thronsen, J. Friis, C. D. Marioara, S. Wenner, A. Bendo, K. Matsuda, R. Holmestad, and S. J. Andersen, Acta Mater. **205**, 116574 (2021).
[30] L. Stemper, M. A. Tunes, P. Dumitraschkewitz, F. Mendez-Martin, R. Tosone, D. Marchand, W. A. Curtin, P. J. Uggowitzer, and S. Pogatscher, Acta Mater. **206**, 116617 (2021).
[31] L. Kovarik and M. Mills, Scr. Mater. **64**, 999 (2011).
[32] L. Kovarik and M. Mills, Acta Mater. **60**, 3861 (2012).
[33] L. Kovarik, P. I. Gouma, C. Kisielowski, S. A. Court, and M. J. Mills, Acta Mater. **52**, 2509 (2004).
[34] L. Kovarik, S. Court, H. Fraser, and M. Mills, Acta Mater. **56**, 4804 (2008).
[35] S. B. Wang, J. H. Chen, M. J. Yin, Z. R. Liu, D. W. Yuan, J. Z. Liu, C. H. Liu, and C. L. Wu, Acta Mater. **60**, 6573 (2012).
[36] C. Pan, Y. Yang, S. Wang, Y. Liu, S. Hu, Z. Wang, and P. Shen, Mater. Des. **187**, 108393 (2020).
[37] Y. Liu, F. Teng, F. Cao, Z. Yin, Y. Jiang, S. Wang, and P. Shen, J. Alloys Compd. **774**, 988 (2019).
[38] S. Wang, Z. Liu, S. Xia, J. Key, and J. Chen, Mater. Charact. **132**, 139 (2017).
[39] M.-J. Yin, J.-H. Chen, S.-B. Wang, Z.-R. Liu, L.-M. Cha, S.-Y. Duan, and C.-L. Wu, Trans. Nonferrous Met. Soc. China **26**, 1 (2016).
[40] J. Liu, S. Yang, S. Wang, J. Chen, and C. Wu, J. Alloys Compd. **613**, 139 (2014).
[41] J. E. Saal, S. Kirklin, M. Aykol, B. Meredig, and C. Wolverton, JOM **65**, 1501 (2013).
[42] G. Imbalzano, A. Anelli, D. Giofré, S. Klees, J. Behler, and M. Ceriotti, J. Chem. Phys. **148**, 241730 (2018).
[43] A. Hjorth Larsen, J. Jørgen Mortensen, J. Blomqvist, I. E. Castelli, R. Christensen, M. Dułak, J. Friis, M. N. Groves, B. Hammer, C. Hargus *et al.*, J. Phys.: Condens. Matter **29**, 273002 (2017).
[44] S. P. Ong, W. D. Richards, A. Jain, G. Hautier, M. Kocher, S. Cholia, D. Gunter, V. L. Chevrier, K. A. Persson, and G. Ceder, Comput. Mater. Sci. **68**, 314 (2013).
[45] P. Giannozzi, S. Baroni, N. Bonini, M. Calandra, R. Car, C. Cavazzoni, D. Ceresoli, G. L. Chiarotti, M. Cococcioni, I. Dabo *et al.*, J. Phys.: Condens. Matter **21**, 395502 (2009).
[46] J. P. Perdew, K. Burke, and M. Ernzerhof, Phys. Rev. Lett. **77**, 3865 (1996).
[47] J. D. Pack and H. J. Monkhorst, Phys. Rev. B **16**, 1748 (1977).
[48] M. Methfessel and A. T. Paxton, Phys. Rev. B **40**, 3616 (1989).
[49] P. E. Blöchl, Phys. Rev. B **50**, 17953 (1994).
[50] A. Dal Corso, Comput. Mater. Sci. **95**, 337 (2014).
[51] G. Prandini, A. Marrazzo, I. E. Castelli, N. Mounet, and N. Marzari, npj Comput. Mater. **4**, 72 (2018).
[52] S. P. Huber, S. Zoupanos, M. Uhrin, L. Talirz, L. Kahle, R. Häuselmann, D. Gresch, T. Müller, A. V. Yakutovich, C. W. Andersen *et al.*, Sci. Data **7**, 300(2020).
[53] M. Uhrin, S. P. Huber, J. Yu, N. Marzari, and G. Pizzi, Comput. Mater. Sci. **187**, 110086 (2021).
[54] D. Marchand and W. Curtin, Materials Cloud 2021.106 (2021), doi: 10.24435/materialscloud:z9-24.
[55] A. Singraber, T. Morawietz, J. Behler, and C. Dellago, J. Chem. Theory Comput. **15**, 3075 (2019).
[56] J. Behler, Int. J. Quantum Chem. **115**, 1032 (2015).
[57] M. W. Mahoney and P. Drineas, Proc. Nat. Acad. Sci. USA **106**, 697 (2009).
[58] A. Singraber, J. Behler, and C. Dellago, J. Chem. Theory Comput. **15**, 1827 (2019).
[59] I. Goodfellow, Y. Bengio, and A. Courville, *Deep Learning* (MIT Press, Boston, 2016).

[60] L. Luttmann and P. Mercorelli, in *2021 25th International Conference on System Theory, Control and Computing, ICSTCC 2021 - Proceedings*, April (2021), pp. 234–241.
[61] S. Plimpton, J. Comput. Phys. **117**, 1 (1995).
[62] F. Musil, M. J. Willatt, M. A. Langovoy, and M. Ceriotti, J. Chem. Theory Comput. **15**, 906 (2019).
[63] C. R. Harris, K. J. Millman, S. J. van der Walt, R. Gommers, P. Virtanen, D. Cournapeau, E. Wieser, J. Taylor, S. Berg, N. J. Smith *et al.*, Nature (London) **585**, 357 (2020).
[64] F. Pedregosa, G. Varoquaux, A. Gramfort, V. Michel, B. Thirion, O. Grisel, M. Blondel, P. Prettenhofer, R. Weiss, V. Dubourg *et al.*, J. Mach. Learn. Research **12**, 2825 (2011).
[65] T. Kluyver, B. Ragan-kelley, F. Pérez, B. Granger, M. Bussonnier, J. Frederic, K. Kelley, J. Hamrick, J. Grout, S. Corlay *et al.*, *Positioning and Power in Academic Publishing: Players, Agents and Agendas*, 87 (2016).
[66] A. Stukowski, Modell. Simul. Mater. Sci. Eng. **18**015012 (2010).
[67] J. D. Hunter, Comput. Sci. Eng. **9**, 90 (2007).
[68] See Supplemental Material at http://link.aps.org/supplemental/10.1103/PhysRevMaterials.6.053803 for a complete report comparing results before and after secondary training.
[69] Y. Zuo, C. Chen, X.-G. Li, Z. Deng, Y. Chen, J. Behler, G. Csányi, A. V. Shapeev, A. P. Thompson, M. A. Wood, and S. P. Ong, J. Phys. Chem. A **124**, 731 (2020).
[70] D. E. Dickel, M. I. Baskes, I. Aslam, and C. D. Barrett, Modell. Simul. Mater. Sci. Eng. **26**, 045010 (2018).
[71] C. Schran, K. Brezina, and O. Marsalek, J. Chem. Phys. **153**, 104105 (2020).
[72] O. I. Gorbatov, A. Y. Stroev, Y. N. Gornostyrev, and P. A. Korzhavyi, Acta Mater. **179**, 70 (2019).
[73] G. Leyson, L. Hector, and W. Curtin, Acta Mater. **60**, 3873 (2012).
[74] V. Vaithyanathan, C. Wolverton, and L. Q. Chen, Acta Mater. **52**, 2973 (2004).
[75] Z. Liu, J. Chen, S. Wang, D. Yuan, M. Yin, and C. Wu, Acta Mater. **59**, 7396 (2011).
[76] H. Perlitz and A. A. Westgren, Chem. Miner. Geol. **16B**, 13 (1943).
[77] C. Wolverton, Acta Mater. **49**, 3129 (2001).
[78] C. Cayron, Acta Crystallogr. Sect. A **62**, 21 (2006).
[79] C. Cayron, J. Appl. Crystallogr. **40**, 1179 (2007).
[80] B. Yin, Z. Wu, and W. Curtin, Acta Mater. **123**, 223 (2017).
[81] L. van Der Maaten and G. E. Hinton, J. Mach. Learn. Research, **9**, 2579 (2008).